AD_____

Award Number: DAMD17-97-1-7053

TITLE: Response of Breast Cancer Cells to Hormonal Therapy;
       Quantitative in vivo NMR Studies

PRINCIPAL INVESTIGATOR: Douglas S. Clark, Ph.D.

CONTRACTING ORGANIZATION: University of California
                          Berkeley, California 94720

REPORT DATE: September 2000

TYPE OF REPORT: Final

PREPARED FOR: U.S. Army Medical Research and Materiel Command
               Fort Detrick, Maryland 21702-5012

DISTRIBUTION STATEMENT: Approved for Public Release;
                        Distribution Unlimited

The views, opinions and/or findings contained in this report are
those of the author(s) and should not be construed as an official
Department of the Army position, policy or decision unless so
designated by other documentation.

20010216 111

REPORT DOCUMENTATION PAGE		*Form Approved* *OMB No. 074-0188*

Public reporting burden for this collection of information is estimated to average 1 hour per response, including the time for reviewing instructions, searching existing data sources, gathering and maintaining the data needed, and completing and reviewing this collection of information. Send comments regarding this burden estimate or any other aspect of this collection of information, including suggestions for reducing this burden to Washington Headquarters Services, Directorate for Information Operations and Reports, 1215 Jefferson Davis Highway, Suite 1204, Arlington, VA 22202-4302, and to the Office of Management and Budget, Paperwork Reduction Project (0704-0188), Washington, DC 20503

1. AGENCY USE ONLY (Leave blank)	2. REPORT DATE September 2000	3. REPORT TYPE AND DATES COVERED Final (15 Aug 97 – 14 Aug 00)	

4. TITLE AND SUBTITLE Response of Breast Cancer Cells to Hormonal Therapy; Quantitative in vivo NMR Studies	5. FUNDING NUMBERS DAMD17-97-1-7053

6. AUTHOR(S) Douglas S. Clark, Ph.D.	

7. PERFORMING ORGANIZATION NAME(S) AND ADDRESS(ES) University of California Berkeley, California 94720 E-MAIL: clark@cchem.berkeley.edu	8. PERFORMING ORGANIZATION REPORT NUMBER

9. SPONSORING / MONITORING AGENCY NAME(S) AND ADDRESS(ES) U.S. Army Medical Research and Materiel Command Fort Detrick, Maryland 21702-5012	10. SPONSORING / MONITORING AGENCY REPORT NUMBER

11. SUPPLEMENTARY NOTES

12a. DISTRIBUTION / AVAILABILITY STATEMENT Approved for public release; distribution unlimited	12b. DISTRIBUTION CODE

13. ABSTRACT *(Maximum 200 Words)*

Our research is directed at determining the specific metabolic pathways and the individual reactions affected by estrogen and tamoxifen in both estrogen receptor-positive (ER+) and estrogen receptor-negative (ER-) breast cancer cells through the use of novel NMR methodology and quantitative analysis. In this award period, we have quantified the effect of estrogen on metabolic fluxes in ER+ cells. This was accomplished using a comprehensive metabolic model and NMR data from cell extracts. The model was further refined to allow for the incorporation of isotopomer, or multiply-labeled, metabolite data. Microcarrier culture, flask, and roller bottle studies were continued in order to expand the methodology used to quantify breast cancer cell metabolism under varied treatment conditions.

14. SUBJECT TERMS Breast Cancer			15. NUMBER OF PAGES 117
			16. PRICE CODE

17. SECURITY CLASSIFICATION OF REPORT Unclassified	18. SECURITY CLASSIFICATION OF THIS PAGE Unclassified	19. SECURITY CLASSIFICATION OF ABSTRACT Unclassified	20. LIMITATION OF ABSTRACT Unlimited

NSN 7540-01-280-5500

Standard Form 298 (Rev. 2-89)
 Prescribed by ANSI Std. Z39-18
 298-102

Table of Contents

        Forbes, N., *et. al.* "Effect of Estrogen on Intracellular Metabolic Fluxes in MCF7
    Human Breast Cancer Cells."

        Forbes, N., *et. al.* "Using Isotopomer Path Tracing to Quantify Metabolic Fluxes
    in Pathway Models Containing Reversible Reactions."

        Wicklund, K., *et. al.* "Effects of Hypoxia on Response to Tamoxifen in MCF7 Human
    Breast Cancer Cells."

INTRODUCTION

Breast cancer, the most prevalent cancer among women, has proven to be a devastating disease. The pain of being diagnosed with the disease is compounded by the lack of a definitive treatment. Currently, the most widely used post-operative hormonal therapeutic is the antiestrogen tamoxifen (TAM). TAM acts at least in part as a competitive inhibitor of estrogen, a hormone which signals cell growth in breast cells. Although effective in postmenopausal patients with estrogen receptor-positive (ER+) tumors, its effectiveness in premenopausal patients and in patients with estrogen receptor-negative (ER-) tumors is substantially lower. Additionally, TAM resistance and cancer recurrence strikes almost all patients with advanced breast cancer undergoing TAM therapy. The serious limitations of this current treatment highlight the need for a greater understanding of both estrogen and TAM action.

A consequence of anti-cancer therapy is an alteration of carbon flows through metabolic pathways. Changes in metabolic fluxes allow cells to provide cellular components to accommodate increased growth. In human breast cancer cells, increased growth and consequent metabolic changes are initiated by estrogen binding to the estrogen receptor. Conversely, TAM is a cytostatic drug which appears to compete with endogenous estrogen for binding to the ER, preventing communication of the growth signal. The effect of this broken communication on metabolism is presently not known. The proposed research uses novel methodology to identify the specific metabolic pathways and the individual metabolic reactions affected by estrogen and TAM in both ER+ and ER- cells. The metabolic effects of these agents, manifested as changes in metabolic fluxes, will be quantified with the aid of NMR techniques. This will enable a description of the relationship between primary metabolism and growth of cells in response to estrogen and TAM treatment to be developed. This new information will help guide the development of new therapies and new therapeutic agents for arresting the metabolism of breast cancer cells and tumors. During the award period, we have made significant progress toward all three goals. Additional experiments to determine the metabolic requirements of ER+ MCF7 cells have been performed in microcarrier culture. Microcarrier culture and roller bottle studies were performed in order to develop and demonstrate the ability to quantify breast cancer cell metabolism under varied treatment conditions. Metabolic fluxes were calculated for estrogen-rescued cells using NMR data from cell extracts and our metabolic model. We have determined that flux analysis using cell extract NMR data is significantly more accurate than that using in vivo data; thus all flux determinations were based on cell extract data.

BODY

The Statement of Work in the original proposal is included below. References to appended manuscripts are included.

Task 1: Months 1-2: Serially wean MCF7 ER+, MCF7 ER-, and T47D ER+ cells to 2% serum. *Concerns were raised about the use of low levels of serum. MCF7 and T47D cell lines are being maintained in 5% serum.*

Task 2: Months 2-5: Implement more precise analytical control and monitoring capabilities of existing hollow fiber bioreactor (HFBR) support apparatus. *A more robust temperature control algorithm implementing cascade control has been created. This controller is capable of maintaining the desired set point ($37\ ^\circ C$) plus or minus $0.1^\circ C$. However, this system will not be used since data obtained from batch extraction experiments afford significantly higher accuracy. In an extraction experiment it is possible to obtain a 100-fold increase in NMR sensitivity. An experiment takes one week as opposed to three months and can test more than 6 conditions as opposed to 1 in an HFBR.*

Task 3: Months 5-6: Treat HFBR with attachment factors and test cell growth. *T47D cells were grown in an HFBR for 3 months at which point the cells where removed by trypsinization. Both NMR and culturing techniques indicated that there was little viability in the 5g cell pellet. A modified HFBR would be needed to attain a higher viable cell density. To overcome the difficulties with the HFBR apparatus, roller bottles are used to obtain the necessary inputs for flux analysis.*

Task 4: Months 7-8: Perform growth studies to determine cerulenin concentration to be used in HFBR experiments. *This task has been completed. Please see appendix A for the manuscript containing complete details.*

Task 5: Month 9: Inject treated HFBR with ER+ MCF7 cells and allow them to grow to high density. *See Task 3.*

Task 6: Months 10-14: Execute serial step changes in medium composition, such as TAM concentration and ^{13}C-labeled metabolites, while continually measuring internal and external metabolites. *Serial step changes were not performed, but equivalent information was obtained, please see appendix A.*

Task 7: Month 15-16: Perform cell extract experiments to confirm spectral assignment of metabolites. *As was described in Materials and Methods, the extraction technique proved to be more beneficial than expected. The ability to detect isotopic distribution by ^{13}C-NMR measurements of extracts prompted us to use cell extract methodology for all subsequent experiments. Please see appendix A for detailed information.*

Task 8: Months 17-18: Perform data analysis. Check for inconsistencies with existing metabolic model. *It was possible to perform this task with ^{13}C-NMR extract measurements. Please see appendix B for a complete description of methodology.*

Task 9: Month 19: Inject treated HFBR with ER+ T47D cells and allow to grow to high density. *See task 3.*

Task 10: Months 20-28: Repeat tasks 6-8 but for the T47D cell line. *Could not complete in the allotted time.*

Task 11: Month 28: Inject treated HFBR with ER- MCF7 cells and allow to grow to high density. *See task 3.*

Task 12: Months 29-36: Repeat tasks 6-8 but for the ER- cell line. *Could not complete in the allotted time.*

Additionally, experiments were carried out to investigate the effect of TAM on metabolism under hypoxic conditions. Please see appendix C for details.

KEY RESEARCH ACCOMPLISHMENTS

- Identified key operative metabolic pathways in ER+ MCF7 breast cancer cells

- Developed novel methodology employing NMR data, including isotopomers, from cell extracts and a metabolic model to calculate intracellular fluxes

- Used this methodology to characterize metabolic responses of MCF7 cells to estrogen and tamoxifen

- Designed microcarrier culture apparatus to allow for easy manipulation of culture environment

- Used microcarrier culture apparatus to investigate the effects of TAM on MCF7 cells under physiologically-relevant oxygen tensions

REPORTABLE OUTCOMES

Manuscripts, Abstracts, Presentations

Forbes, N.S., Blanch, H.W. and Clark, D.S. "Metabolic Flux Analysis to Characterize the Response of Human Breast Cancer Cells to Hormones," poster presented at the Metabolic Engineering II Meeting, Elman, Germany, October 25 1998.

Forbes, N.S., Blanch, H.W. and Clark, D.S. "The Metabolic Response of Breast Cancer Cells to Estradiol" presented at the American Institute of Chemical Engineers National Meeting, Dallas, TX, November 1, 1999.

Forbes, N.S., Blanch, H.W. and Clark, D.S. "Analysis of Metabolic Fluxes in Mammalian Cells". In: Bioreaction Engineering: Modelling and Control. Eds. Schugerl, K., Bellgardt, K. Springer-Verlag, Berlin, Germany, in press.

Forbes, N.S., Blanch, H.W. and Clark, D.S. "Effect of Estrogen on Intracellular Metabolic Fluxes in MCF7 Human Breast Cancer Cells." Manuscript in preparation. See Appendix A.

Forbes, N.S., Blanch, H.W. and Clark, D.S. "Using Isotopomer Path Tracing to Quantify Metabolic Fluxes in Pathway Models Containing Reversible Reactions." Submitted to *Biotech. Bioeng.* See Appendix B.

Wicklund, K.A., Blanch, H.W. and Clark, D.S. "Characterization of MCF7 human breast cancer cells in microcarrier culture: Effects of hypoxia," presented at the American Chemical Society National Meeting, San Francisco, CA, March 29, 2000.

Wicklund, K.A., Blanch, H.W. and Clark, D.S. "Characterization of MCF7 human breast cancer cells in microcarrier culture: Effects of glucose and hypoxia" presented at the American Institute of Chemical Engineers National Meeting, Dallas, TX, November 4, 1999.

Wicklund, K.A., Blanch, H.W. and Clark, D.S. "Characterization of Human Breast Cancer Cells in Microcarrier Culture: Effects of Glucose and Oxygen," poster presented at the Whitaker Foundation Annual Meeting, La Jolla, CA, August 18, 1999.

Wicklund, K. A., Blanch, H.W. and Clark, D.S. "Characerization of Human Breast Cancer Cells in Microcarrier Culture," presented at the American Chemical Society National Meeting, Anaheim, CA, March 25, 1999.

Wicklund, K.A., Blanch, H.W. and Clark, D.S. "Effects of Hypoxia on Response to Tamoxifen in MCF7 Human Breast Cancer Cells." Manuscript prepared for submission to *Cancer Research.* See Appendix C.

Degrees Obtained
Ph.D. awarded to Neil Forbes

CONCLUSIONS

In summary, we have developed advanced methodology that has allowed us to investigate the metabolic consequences of estrogen and tamoxifen treatment. We have identified for the first time isotopomers following 1-^{13}C glucose treatment, which was enabled by advances in the proposed technique. We have also developed an algorithm to analyze isotopomer data that is fast, general, and increases the accuracy and extent of flux calculations. These improvements in methodology have allowed us to quantify more completely internal metabolic fluxes in ER+ human breast cancer cells following estrogen rescue. Results from this analysis have confirmed our hypothesis about the action of estrogen. Specifically, increases in the pentose phosphate pathway, glutaminolysis, and flux through pyruvate carboxylase were observed following estrogen stimulation. We have also completed preliminary investigations using the fatty acid synthase inhibitor, cerulenin. Finally, we have developed a cell culture apparatus that allows for the adjustment of oxygenation. This apparatus was used to study, for the first time, the effect of TAM under physiologically relevant oxygen tensions.

Effect of Estrogen on Intracellular Metabolic Fluxes in MCF7 Human Breast Cancer Cells

N. Forbes, H. Blanch, and D. Clark, Dept. of Chemical Engineering, University of California-Berkeley CA 94720

Abstract

Carbon fluxes through the pathways of primary and secondary metabolism were calculated from ^{13}C-NMR data and extracellular fluxes using a comprehensive model. Fractional enrichments and isotopomer fractions were measured by NMR and interpreted by a novel algebraic reduction method. The flux results showed that, in MCF7 ER+ cells, estrogen treatment significantly increased glycolysis, glutaminolysis and the pentose phosphate pathway. Both the malate-aspartate shuttle and intra-mitochondrial malic enzyme are inactive in these cancer cells.

Introduction

As a more complete picture of the genetic and enzymatic composition of cells becomes apparent, there is a growing need to describe how cellular regulatory elements interact with the cellular environment to affect cell physiology. Concurrently measuring multiple metabolic pathways and their interactions describes intracellular regulatory mechanisms including changes in enzyme and substrate concentrations, enzyme activation or inhibition, and ultimately genetic control. The response of the central metabolism of MCF7 breast cancer cells to estradiol was quantified to characterize their phenotype and identify potential enzyme targets for drugs to treat tumors unresponsive to anti-estrogen therapy.

Carbon fluxes were calculated from ^{13}C-NMR isotopomer data using a rapid and novel solution method that employs *isotopomer path tracing* to significantly reduce the

number of variables and hence the solution time. Reversible reactions were described by a new parameter, the *association factor*, which scales hyperbolically with the rate of metabolite exchange. The automated solution method evaluated numerous models and generated confidence intervals for the flux results. The method is capable of determining the intracellular metabolic fluxes in all types of cells, and can incorporate any hypothesized pathway model. The pathway model utilized in this work contained seven independent intracellular branches in addition to mitochondrial compartmentalization.

As a more complete picture of the genetic and enzymatic composition of cells becomes apparent, there is a growing need to describe how cellular regulatory elements interact with the cellular environment to affect cell physiology. Concurrently measuring multiple metabolic pathways and their interactions describes intracellular regulatory mechanisms including changes in enzyme and substrate concentrations, enzyme activation or inhibition, and ultimately genetic control. The response of the central metabolism of MCF7 breast cancer cells to estradiol was quantified to characterize their phenotype and identify potential enzyme targets for drugs to treat tumors unresponsive to anti-estrogen therapy.

Carbon fluxes were calculated from ^{13}C-NMR isotopomer data using a rapid and novel solution method that employs *isotopomer path tracing* to significantly reduce the number of variables and hence the solution time. Reversible reactions were described by a new parameter, the *association factor*, which scales hyperbolically with the rate of metabolite exchange. The automated solution method evaluated numerous models and generated confidence intervals for the flux results. The method is capable of determining the intracellular metabolic fluxes in all types of cells, and can incorporate any

hypothesized pathway model. The pathway model utilized in this work contained seven independent intracellular branches in addition to mitochondrial compartmentalization.

Experimental protocol

General culture techniques MCF7 breast cancer cells were grown in Dulbecco's modified Eagle's medium with 5% fetal bovine serum (FBS, Sigma lot #98H8407). Experiments were performed in 850 cm^2 roller bottles to maximize cell number and hence intensify the NMR signal. Bottles were turned at 1 RPM and were kept at 37 °C. The headspace of each bottle was intermittently replenished with a 5% CO_2/air mixture. Isotopically-enriched media was prepared by addition of 1 g/l (5.56 mM) 1-^{13}C glucose to base DME medium (Sigma, #D5030) containing standard concentrations of glutamine, pyruvic acid, phenol red and sodium bicarbonate.

Experiment procedure Eighteen roller bottles were seeded at a density of 40,000 cells/cm^2, and were grown in standard DMEM with 5% FBS for 24 hours and DMEM with 5% containing 5 μM TAM for the next 96 hours. Estrogen rescue, the halting of cell growth with tamoxifen followed by synchronous stimulation with estradiol (E2), amplifies the estrogen response. The bottles were collected into six groups of equal average density for each of the treatment regimes: control, E2, cerulenin (Cer), oxamate (Ox), E2 + Cer, and E2 + Ox. On the fifth day the bottles were fed 1-^{13}C glucose-containing media and the various combinations of 0.5 μM estradiol, 26.9 μM cerulenin, and 50 mM oxamate. Every eight hours for the next 36 hours, a 0.5 ml sample was removed from each bottle, and stored at −4°C. After this 36-hour period a final sample was taken, the intracellular metabolites were extracted, and the solid cell matter was collected for cell number determination.

Concentration profiles of extracellular metabolites Extracellular fluxes in batch roller bottle cultures were measured as changes in the concentration of extracellular metabolites as a function of time. Glucose, lactate, glutamate, and glutamine concentrations were determined enzymatically with a *YSI* biochemistry analyzer. Amino acid concentrations were determined by high-pressure liquid chromatograph following phenylisothiocyanate derivatization. Ammonia concentration was determined with an *Orion* ammonia electrode connected to a *Beckman* pH/ISE meter.

Perchloric acid extraction The intracellular ^{13}C-containing metabolites were isolated from the cultures at the end of the experiment using the perchloric acid (PCA) extraction similar to that described by Damadian (1981), Degani et al. (1991), Portais et al. (1993), and Metz and Dunphy (1996). Media was removed from the culture bottles. The cell layer was washed with phosphate buffered saline, and treated with 10 ml of ice cold 5% PCA. The bottles were turned at 3 RPM at –4°C for 10 minutes. The lysate was removed, neutralized to between pH 7 and 8 with 2.5 ml 2M K_2CO_3, centrifuged for 5 minutes at 4000 RPM, flash frozen with liquid nitrogen, and lyophilized at –50°C and 40×10^{-3} mBar.

Cell number determination The solid cell material remaining in the roller bottles following lysis was physically removed with scrapers, washed with 50 ml of de-ionized water, centrifuged, and washed twice with 1 ml of de-ionized water. One ml water was added, and the solid material was dried in glass weigh vessels at 105°C for 48 hours. Extraction dry weight was correlated to cell number by an unpublished calibration utilizing *Coulter* cell counting. The correlation between dry weight and cell number was:

$$\text{Χελλ νυμβερ (ιν μιλλιονσ)} = 3.90 \; \xi \; \mu\alpha\sigma\sigma \; o\phi \; \chi\epsilon\lambda\lambda \; \sigma o\lambda\iota\delta\sigma \; (\mu\gamma) \quad 8.28. \quad (1)$$

NMR sample preparation To reduce the amount of insoluble potassium perchlorate, the lyophilized extracts were dissolved in 650 μL de-ionized water, centrifuged for 10 minutes at 3000 RPM, and re-lyophilized. For NMR analysis, the extracts were dissolved in 250 μl of a deuterium oxide solution containing 0.5% sodium azide, and 90.27 mM ethylene glycol, a calibration standard that produces a single peak at 62.5 ppm. Extracts were loaded into Shigemi NMR tubes that double the signal by requiring half the volume of regular NMR tubes.

Acquisition parameters All ^{13}C-NMR spectra of the cell extracts were acquired at 125 MHz and were signal averages of 5600 scans. Ninety-degree pulses of duration 8 μsecs and an inter-pulse delay of six seconds were used, which is more than four times the longest spin-lattice relaxation time (1.37) of a nucleus in the extract. Samples were held constant at 301°K to prevent peaks from drifting during the long acquisition time. The nuclear Overhauser enhancement (NOE) was compensated by comparison to a standard acquired without perpetual proton decoupling. Isotopically labeled media samples, from the point of extraction, were similarly analyzed for 40 scans with an inter-pulse delay of six seconds.

The identities of the peaks in the extract spectra were determined by direct addition of concentrated standards to the extracts. Surprisingly, the peaks corresponding to carbon nuclei in the standard and extract solutions were shifted as far as 2.4 ppm upfield from their location in spectra of the standards alone. Ensemble isotopomer concentrations, which are the sum of the concentrations of all isotopomers with an identical pattern of ^{13}Cs over one bond length, were determined by comparison to the ethylene glycol standard.

Simulation The experimental data (extracellular fluxes and isotopomer fractions) is converted to intracellular fluxes by a two-stage algorithm described in Forbes et al., 2000. The first stage interprets the flow of isotope through the pathway model, which is represented mathematically by a stoichiometric matrix, using atom-mapping matrices (Zupke and Stephanopoulos, 1994), which describe the transition of substrate atoms to product atoms. The second stage is an iterative simulation that computes the values of the intracellular fluxes following initialization with a set of guessed fluxes and simulation parameters. Simulated annealing was used to determine approach the global solution of the non-linear relation between isotopomer pattern and intracellular fluxes. Each simulation was repeated ten times, included 10,000 iterations, and used an annealing constant of 1000, which defines when the dead band is at half its initial value (Schmidt et al., 1999).

Monte Carlo simulation Each set of simulations was repeated 500 times with an alternate input data set derived from the measurement errors. The deviation in the resultant set of fluxes is the confidence in the determined intracellular fluxes.

Results

The algorithm used to determine the internal metabolic fluxes (Forbes, et al., 2000) required two types of experimental measurements, extracellular fluxes and isotopomer fractions. The set of extracellular fluxes includes both the production and consumption rates of metabolites contained in the culture medium. They are the most significant interaction of the cells with their external environment and easiest to measure. An isotopomer is a metabolite with a specific labeling pattern, of which there are 2^n in a

molecule with n carbon atoms. The values of the isotopomer fractions are dependent on the intracellular fluxes, and are the means by which the machinery of the interior of the cell was investigated.

The experimental procedure was created to determine these two types of measurements for a single population of cells. After feeding roller bottles of MCF7 breast cancer cells media containing 1-^{13}C glucose, samples were taken every eight hours to determine rates of consumption and production. After 36 hours, the cytoplasm of the cells was extracted using perchloric acid. These extracts were analyzed by NMR to determine the isotopic pattern of the intracellular metabolites.

The metabolic effects of estradiol were investigated using estrogen rescue in combination with the two enzyme inhibitors, cerulenin and oxamate. Cerulenin is a specific inhibitor of fatty acid synthase and oxamate is a pyruvate analog that inhibits lactate dehydrogenase. Estrogen rescue, which is the halting of cell growth with tamoxifen followed by synchronous stimulation with estradiol (E2), was used to amplify the estrogen response. The six different experimental regimes were: an untreated control, estrogen rescue (E2), a cerulenin control (Cer), an oxamate control (Ox), estrogen rescue and cerulenin (E2 + Cer), and estrogen rescue and oxamate (E2 + Ox).

Extracellular fluxes were derived from the slope of linear or exponential functions fit to the time profiles of the extracellular metabolites at the time of extraction (152 hours after seeding). For example, Fig. 1 is the time profile of the consumption of glucose and the production of lactate by the estrogen rescued and control bottles. Estradiol clearly and significantly increases the consumption rate of glucose and the production rate of lactate. The other extracellular metabolites that were measured for each of the six

16

different treatment regimes are glutamine, glutamate, alanine, and ammonia. Fluxes are

reported in units of μMole/hr/10^9cell and standards errors were derived from the data of
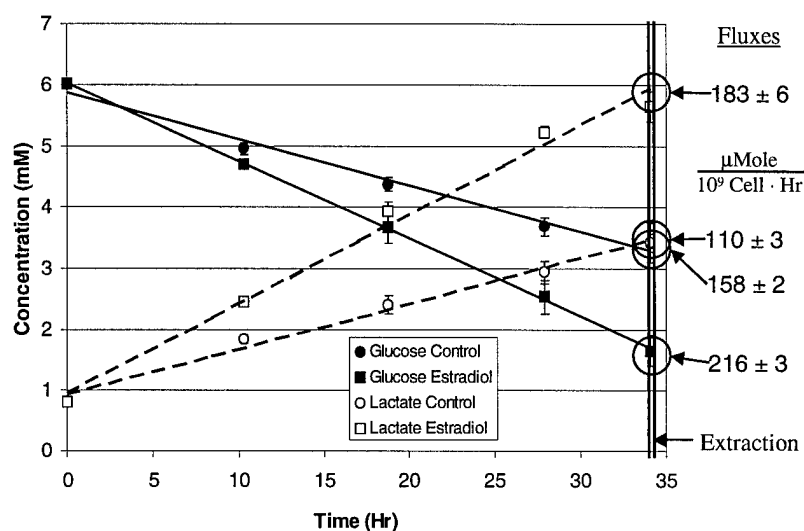
three separate bottles.

Figure 1. Estradiol increases the extracellular fluxes of glucose and lactate

The number of cells at the point of extraction was determined from the dry weight of the

remaining cell solids. The six regimes experienced significantly different growth.

Estrogen rescue increased the growth rate of the control regardless of the presence of

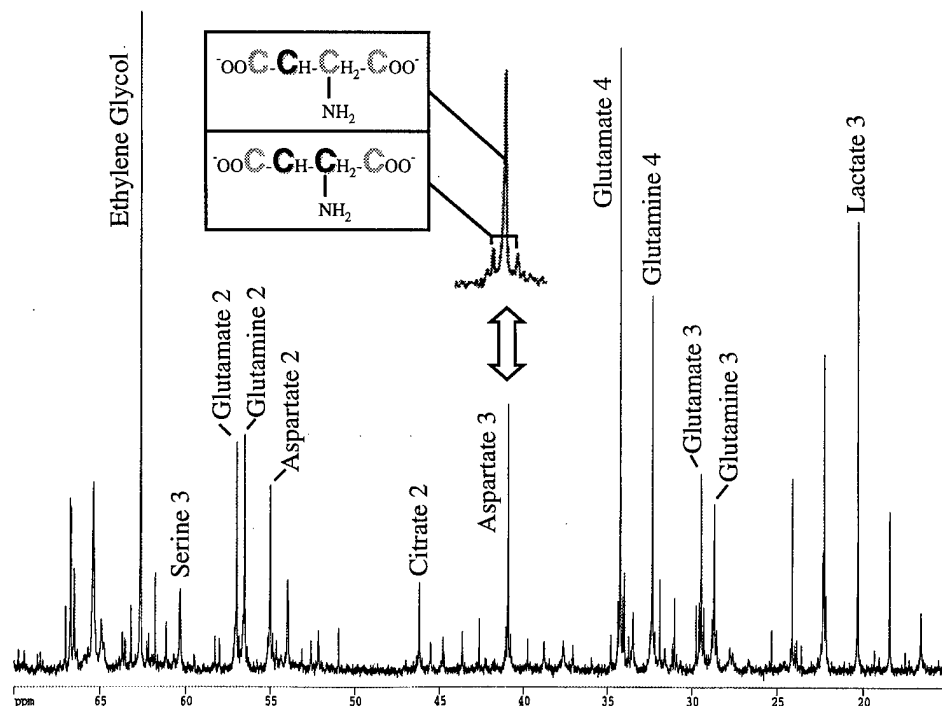cerulenin or oxamate, and as expected, the cerulenin and oxamate controls had slower

growth.

Figure 2. Representative ^{13}C-NMR spectrum from one of the control extracts

The inset is an enlargement of the aspartate3 group of peaks, which shows how fine structure (in this case the two isotopomers asp3 and asp 23) was visible in our high-sensitivity spectra. The top of ethylene glycol reference peak (62.5 ppm) was cut off, so that the detail of the metabolite peaks could be seen more clearly.

Figure 2 is representative ^{13}C-NMR spectrum from one of the control bottles. The peaks from the carbon nuclei that were used to calculate intracellular fluxes are indicated. Isotopomer fractions are the ratio of the concentrations of specific patterns of carbon labeling in a metabolite to the total concentration of that metabolite in the extract. Concentration was determined by comparison of peak height to that of the ethylene glycol standard. Metabolites concentrations were determined by HPLC. A single peak in

18

a ^{13}C spectrum represents an ensemble of different isotopomers with a conserved labeling pattern within one bond of the observed nucleus. Triplicate spectra were obtained for each of the six treatment regimes to determine the errors in the isotopomer fractions. In combination with the extracellular fluxes, the isotopomer fractions represent the complete set of data that was input into the solution algorithm to generate intracellular fluxes.

A. Metabolism of MCF7 Cells

Each of the six data sets was run through the solution algorithm 10 times sequentially, with the results from one run used as the initial guesses for the next. This was found to be the fastest way to consistently approach global solutions. Each run consisted of 10,000 iterations. Errors in the intracellular fluxes were determined by Monte Carlo simulation.

Ten different pathway models were generated and tested for goodness of fit to the data. However, only two produced physiologically feasible results. The significance of the ten models is discussed in following sections. One of the two feasible models contained two more independent fluxes, and was more sensitive to the initial guesses. The other more stable model with less independent fluxes quickly approached one answer regardless of the initial guess. The more stable model is shown in Fig. 5.17, and its resultant fluxes are given in Table 5.4. All flux values have units of μMole/hr/10^9cell, except the two association factors α_1 and α_2, which describe the degree of reversibility of the malate-aspartate shuttle and the glutamate transmembrane exchange and are dimensionless. The normalized *distal* association factor is reported. The *proximal* association factor can be calculated from the distal, and is of similar magnitude. In this model, two pairs of fluxes f_{21} and f_{22}, and f_{29} and f_{30} were constrained to be equal, and f_{29}

was constrained to be $0.887 \cdot f_{21}$. The value, 0.887 is the average ratio of aspartate to glutamate in mammalian cell proteins.
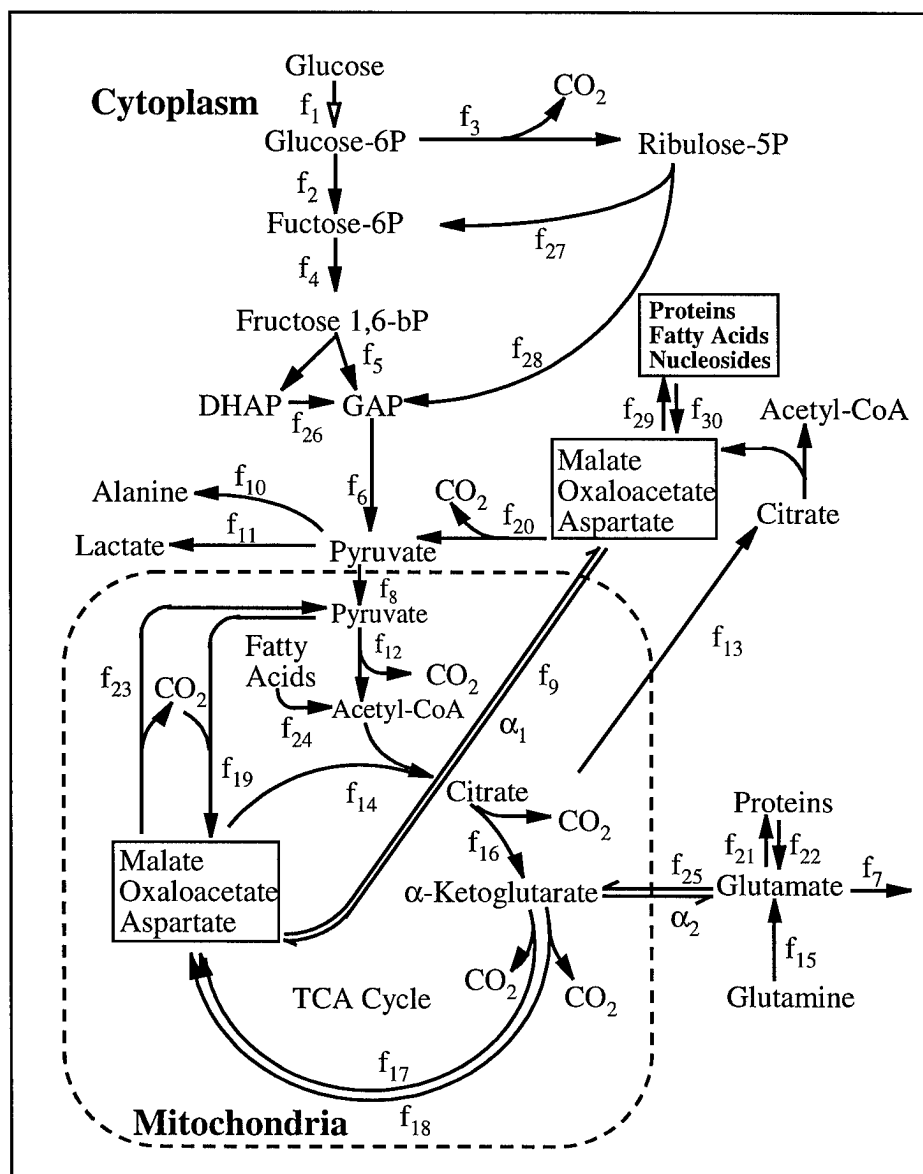

Figure 5.18 Metabolic Pathway Model

Table 5.4 Intracellular Fluxes (mMole/hr/10^9 cell)

		Control	Estradiol	Cerulenin	Oxamate	Cer + E2	Ox + E2
Glucose	f_1	160 ± 11	216 ± 3	186 ± 10	188 ± 12	228 ± 9	196 ± 17
Pentose Phosphate	f_3	8 ± 3	50 ± 1	54 ± 4	85 ± 6	21 ± 5	54 ± 6
Glutamate	f_7	0 ± 0.0	0 ± 0.0	11 ± 0.2	0 ± 0.0	9 ± 0.1	0 ± 0.0
Mal-Asp net flux	f_9	66 ± 6	72 ± 2	81 ± 8	59 ± 11	65 ± 9	66 ± 3
Mal-Asp exchange	α_1	0.0 ± 0.002	0.02 ± 0.008	0.0 ± 0.002	0.18 ± 0.03	0.11 ± 0.02	0.04 ± 0.03
Alanine	f_{10}	11 ± 0.1	12 ± 0.1	8 ± 0.2	11 ± 0.1	9 ± 0.2	13 ± 0.1
Lactate	f_{11}	110 ± 2	183 ± 5	86 ± 4	93 ± 3	146 ± 7	156 ± 2
TCA Cycle	f_{14}	239 ± 24	293 ± 8	282 ± 20	284 ± 22	337 ± 17	270 ± 31
Glutamine	f_{15}	43 ± 3	73 ± 2	34 ± 0.3	40 ± 0.2	51 ± 0.3	66 ± 1.7
Channeling I	f_{17}	180 ± 20	173 ± 4	212 ± 18	209 ± 21	247 ± 19	174 ± 18
Channeling II	f_{18}	102 ± 10	192 ± 4	93 ± 13	115 ± 13	131 ± 16	162 ± 15
Pyr Carboxylase	f_{19}	24 ± 6	0 ± 0.3	59 ± 8	19 ± 13	23 ± 8	0 ± 0.4
Malic Enzyme (ex)	f_{20}	66 ± 6	72 ± 2	81 ± 8	59 ± 11	65 ± 9	66 ± 3
Protein Turnover	f_{21}	260 ± 28	269 ± 8	248 ± 25	144 ± 14	353 ± 22	219 ± 29
Malic Enzyme (in)	f_{23}	0 ± 1.1	0 ± 0.0	0 ± 0.2	0 ± 0.2	0 ± 0.2	0 ± 0.1
Glut Trans net flux	f_{25}	43 ± 2.9	72 ± 1.7	23 ± 0.4	40 ± 0.2	42 ± 0.4	66 ± 1.7
Glut Trans exch	α_2	0.41 ± 0.01	0.34 ± 0.002	0.38 ± 0.01	0.58 ± 0.01	0.32 ± 0.01	0.40 ± 0.01
Ammonia	NH_3	35 ± 1.0	35 ± 0.2	25 ± 0.2	47 ± 4	29 ± 0.5	27 ± 5
Model Error	LSE	12.9 ± 1.3	65.5 ± 0.8	12.2 ± 0.7	45.3 ± 0.9	30.7 ± 1.5	21.2 ± 0.5

Discussion

1. General findings about cancer cell metabolism: The malate-aspartate shuttle and intra-mitochondrial malic enzyme

The results Table 5.4 indicate that intra-mitochondrial malic enzyme (intra-ME) is inactive and the malate-aspartate (mal-asp) shuttle is irreversible. The intra-ME flux (f_{23}) was equal to zero in all six treatments for each of the ten models tested. In the pathway model in Fig 5.18, the mal-asp shuttle is represented by a reversible flux (f_9). The

association factor (α_1) for the mal-asp shuttle was near or equal to zero for all six of the treatment regimes, indicating that the shuttle was irreversible and therefore inactive. Both of these observations led to the hypothesis that connects three unexplained characteristics of cancer cells, aerobic glycolysis, glutaminolysis, and rapid proliferation.

The inactivity of intra-mitochondrial malic enzyme was anticipated because malic enzyme is located in the cytosol in normal epithelial cells (Newsholme and Leech, 1983). The inactivity of intra-ME is significant because of its role in the high glutamine consumption rates seen in many cancer cells. It has been hypothesized that cancer cells preferentially consume and oxidize glutamine to produce ATP, even in the presence of glucose (Eigenbrodt et al., 1985). After glutamine is taken up a cell, it is deamidated to glutamate (f_{15}), transported into the mitochondrial (f_{25}), and oxidized to malate (f_{17}). To completely oxidize the glutamine carbons, intra-ME (f_{23}) would then decarboxylate the malate to pryruvate. The pyruvate is in turn decarboxylated to acetyl-CoA (f_{12}), which commits the glutamine carbons to complete oxidation by the TCA cycle. Without intra-ME activity, TCA cycle metabolites cannot be oxidized inside the mitochondria. Therefore, the activity of the anaplerotic pathways (glutamine consumption and pyruvate carboxylase) must be balanced by fluxes out of the mitochondria, which supply precursors for biosynthetic pathways. Because oxidation of glutamine carbons by transporting them across the mitochondrial membrane twice is inefficient, the teleological purpose of glutamine consumption is most likely to supply biosynthetic precursors.

The malate-aspartate shuttle is a cycle of reactions that transport NADH from the cytosol into the mitochondria. There the NADH is used to generate ATP by oxidizing it to NAD^+. The mal-asp shuttle is composed of four basic steps: the conversion aspartate

into malate in the cytosol, the conversion of malate into aspartate in the matrix of the mitochondria, and the two trans-membrane fluxes of malate and aspartate. The only other means for NADH produced in the cytosol to be transported into the mitochondria is the 3-phosphoglycerate shuttle. This NADH shuttle cannot be measured by ^{13}C-tracer experiments, because it does involve a net carbon flux. However, it is believed to be inactive in most transformed cells (Eigenbrodt et al., 1985).

In the pathway model in Fig 5.18 the mal-asp shuttle is depicted as the single reversible flux, f_9. Because none of the reactions of the mal-asp shuttle rearrange the carbon order, the two transmembrane fluxes of malate and aspartate are isotopically indistinguishable. By modeling the mal-asp shuttle as a single reversible flux, the *direction* of cycling cannot be determined, however the degree of reversibility of this flux does describe the *rate* of cycling. In addition, the transport of citrate out of the mitochondria (f_{13}) does not rearrange carbons and is also isotopically indistinguishable. For this reason all ten models lacked an independent citrate trans-membrane flux. The net flux through f_9 is thus a composite of the aspartate, malate and citrate trans-membrane fluxes. Although it was not possible to determine the absolute composition of the f_9 net flux, it was most likely a combination of all three (malate, aspartate, and citrate) effluxes. Matsuno (1989) showed that when extracted mitochondria from chicken hepatomas were incubated in a glutamine-rich medium, they predominately produced aspartate, malate, citrate, glutamate, and other metabolites.

In the pathway model, the mitochondrial influx (f_{25}) is a composite of the influxes of glutamate, α-ketoglutarate, and glutamine. The composite mitochondrial influx (f_9) and efflux (f_{25}) are connected by two antiport transport systems; one that exchanges α-

ketoglutarate for malate, and one that exchanges glutamate for aspartate (Matsuno, 1987). Therefore the influxes of glutamate and α-ketoglutarate are equal to the effluxes of aspartate and malate, respectively. Glutamine influx occurs passively by an energy-independent process (Campbell and Vorhaben, 1976; Matsuno, 1987). The citrate efflux component of f_9 is therefore equal to the glutamine influx component of f_{25} plus the pyruvate carboxylase flux (f_{19}).

We hypothesize that inactive intra-ME and mal-asp shuttle provide a link between the high cytosolic NADH/NAD$^+$ ratio, the high glutamine consumption rate, and the rapid proliferation rate seen in cancer cells. By taking up glutamate or glutamine and producing aspartate or citrate, the mitochondria of cancer cells reduce the cytosolic NADH/NAD$^+$ ratio and provide biosynthetic precursors. Cytosolic citrate is cleaved into acetyl-CoA and oxaloacetate and similarly, aspartate is deaminated to oxaloacetate. By reducing this oxaloacetate to malate one molecule of NADH is oxidized. Therefore the uptake of glutamine and glutamate has the same effect as a single turn of the mal-asp shuttle; NADH is produced inside the mitochondria and consumed in the cytosol. We hypothesize that cancer cells in a diminished glutamine medium will have an increased lactate production because of an increased cytosolic NADH/NAD$^+$ ratio.

High levels of cytosolic NADH, produced by a stimulated glycolysis, are linked to mitochondrial take up of glutamate and glutamine and the production of biosynthetic precursors. The cytosolic acetyl-CoA produced from citrate by ATP-citrate lyase is utilized in *de novo* lipogenesis and cholesterol synthesis, and the aspartate amide is utilized for purine synthesis. Alternately, the entire aspartate is utilized for pryimidine or protein synthesis.

Alternately, glutamine taken up by a cell can be deamidated and then deaminated to α-ketoglutarate, and transported into the mitochondria in exchange for malate. The exchange of α-ketoglutarate for malate does not reduce cytosolic NADH levels. However, the amine cleaved from the glutamate to produce α-ketoglutarate is used in numerous biosynthetic reactions. Therefore all three of the influx-efflux pairs contribute to biosynthetic pathways, solidifying the connection between glutaminolysis and biosynthesis.

2. *The Effects of Estradiol*

In table 5.4 most of the metabolic fluxes were increased by the addition of 0.5 μM estradiol including, glycolysis (f_1), the pentose phosphate pathway (PPP, f_3) lactate production (f_{11}), the TCA cycle (f_{14}), and glutamine consumption (f_{15}). The increase in the TCA cycle flux indicates that estradiol generally stimulates the metabolism and energy production of these estrogen-responsive breast cancer cells. However estradiol also stimulated pathways specific to the transformed phenotype.

The increase in glucose uptake and lactate production is similar to the Warburg effect, which is an increase in aerobic glycolysis due to transformation. This high rate of aerobic glycolysis has long been a mystery because of the energy and carbon lost due to the production of lactate. However, because aerobic glycolysis is seen in numerous types of rapidly proliferating cells, both healthy and cancerous, the production of lactate is most likely a response critical for proliferation. The evidence in Table 5.4 leads us to hypothesize that lactate production is a secondary effect of an increased production of biosynthetic precursors. This hypothesis, which is similar to those of Eigenbrodt et al. (1985) and Baggetto (1992), is explained in more detail in subsequent sections.

The six-fold increase in the PPP and the doubling of glutamine uptake supports these hypotheses regarding the mechanisms of estradiol induced proliferation. The PPP reduces the cofactor NADP+ to NADPH, which is in turn oxidized to NADP+ in many biosynthetic pathways, including *de novo* lipogenesis and cholesterol synthesis. An increased PPP flux provides additional NADPH, thus supporting increased biosynthetic production. This increased PPP flux was anticipated because the expression of glucose-6-phosphate dehydrogenase (G6PDH), which is the committing enzyme into the PPP, is induced by estradiol (Thomas et al., 1990).

The consumption of glutamine occurs through an anaplerotic pathway, meaning that its activity causes a net increase the concentration of TCA cycle metabolites. These metabolites are excreted from the mitochondria and increase the cytosolic pools of citrate and aspartate, which are precursors for numerous cellular macromolecules. The other major anaplerotic pathway involves pyruvate carboxylase. The activities of the anaplerotic pathways are necessary for proliferation, because they are the only means of producing cytosolic aspartate and citrate. When glutamine is consumed, it is partially oxidized before being excreted from the mitochondria, thereby generating energy as well as increasing precursor pools. This makes it a favorable substrate for rapidly growing cells. An increase in glutamine consumption was anticipated because high rates of glutamine consumption are typical in transformed cells. However, the decrease in pyruvate carboxylase activity was not anticipated. One explanation is that the cells maintained a constant extra-mitochondrial malic enzyme flux. Pyruvate carboxylase activity was reduced when glutamine consumption increased.

3. The Effects Cerulenin

The two enzyme inhibitors, cerulenin and oxamate, were used to test whether either fatty acid synthase (FAS) or lactate dehydrogenase (LDH) are key enzymes, induced by estradiol, which stimulate proliferation. The two controls with cerulenin and oxamate alone were run to identify how their addition would affect metabolism. The two combinations containing either cerulenin and estradiol or oxamate and estradiol were examined to determine whether the inhibitors would return the metabolism of the estradiol stimulated cells to the level of the control.

Unfortunately, neither of the inhibitors had a unique effect on the metabolism of the cells. While this eliminated our ability to test the regulatory role of the enzymes FAS and LDH, certain conclusions regarding the metabolism of these cells can be drawn from the flux results. There are three reasons that the enzyme inhibitors affect the entire metabolic pattern. Oxamate is not a specific inhibitor of LDH. Because it is an analog of pyruvate, it may inhibit all enzymes that act on pyruvate. Cerulenin is believed to be a specific inhibitor of FAS (Kuhajda et al., 1994). One of the major advancements of Metabolic Control Theory (Kacser and Burns, 1979; Kacser, 1983; Fell, 1992) was the notion that fluxes through most of the pathways of metabolism are tightly connected. A small change in the flux through one pathway may significantly affect the flux through another, potentially in a manner difficult to predict *a priori*. Cerulenin and oxamate may be specific for FAS and LDH, but altering the flux through these two enzymes may alter many other fluxes. The third explanation is that these two inhibitors stress the cells, causing metabolic changes unrelated to the expected modes of action. One conclusion that can be drawn is that both of these inhibitors, for whatever reason, do not return

27

estradiol treated cells to the metabolism of the control cells. Therefore the actions of cerulenin and oxamate do not oppose the metabolic effects of estradiol.

The most significant effect of cerulenin was a dramatic increase in the glutamate production rate. All of the cultures not treated with cerulenin had a very low glutamate uptake rate whereas those treated with cerulenin, excreted glutamate. At the same time cerulenin decreased the rate of glutamine uptake. Estradiol did not affect glutamate excretion, but did increase glutamine uptake. Some glutamine consumed by these cells was converted into cytosolic citrate by the mitochondria and used for fatty acid synthesis. Inhibiting fatty acid synthesis with cerulenin resulted in a build up of TCA cycle intermediates and cellular glutamate, which resulted in lower rates of glutamate excretion.

Cerulenin did not significantly affect either the pentose phosphate pathway (PPP) or the biosynthetic/biodegradation fluxes. Fatty acid synthesis may have been a small enough fraction of the set of biosynthetic/biodegradation (f_{29} and f_{30}) fluxes that its inhibition did not affect the whole. Similarly, the demand on the PPP caused by fatty acid synthesis may be only a fraction of the NADPH requirement.

4. The Effects of Oxamate

The most significant effects of oxamate are an increase in ammonia production and PPP flux, and a decrease in lactate secretion. The decrease in LDH activity is a predicted effect of oxamate. Because oxamate did not decrease the glucose uptake rate, we can hypothesize that accumulation of either pyruvate or lactate does not reduce glycolysis, which is more like controlled by phosphofructokinase (PFK)-I. Dang and Semenza (1999) speculated that an increased LDH-A activity was the cause of aerobic

28

glycolysis and increased proliferation in cancer cells. This hypothesis is not supported by the results of oxamate inhibition. However, the observation that LDH activity returned to the level of the control cells when they were treated with both oxamate and estradiol, supports the observation that estradiol stimulated LDH expression.

The TCA cycle flux is minimally affected by oxamate, which is a pyruvate analog and may have inhibited pyruvate dehydrogenase (PDH), the step that commits pyruvate carbons to oxidation in the mitochondria. The very small reduction in alanine production by the oxamate treated cells hints that oxamate inhibits alanine aminotransferase. Cells preferentially excrete excess nitrogen as either ammonia or alanine. Cancer cells have more excess nitrogen because of their increased glutamine consumption. The increase in the PPP in the slower growing oxamate treated cells is surprising. One explanation is that the toxic effects of the oxamate cause a stress response that requires NADPH.

5. The Effects of Various Models on Flux Calculations

Ten different models of metabolic pathways were tested against the six sets of data presented in tables 5.2 and 5.3. Most of these models varied in how the biosynthetic and biodegradation pathways (f_{21}, f_{22}, f_{29}, and f_{30}) were related. These four fluxes served two purposes. First, they are lumped paths summing the production and breakdown of proteins, fatty acids and nucleosides. Secondly, they were required mathematically to explain the measured isotopomer fractions.

Although only two of the ten models produced physiologically reasonable results, the apparent failures of the other eight models still contributed metabolically relevant information. The model, which was used to produce the results in table 5.4, was the most constrained. The biosynthetic and biodegradation rates of glutamate (f_{21}, f_{22}) and

aspartate (f_{29}, f_{30}) were constrained to be equal. Because it was assumed that the production and degradation of protein was greater than that of either fatty acids or nucleosides, the ratio of aspartate (f_{29}) to glutamate incorporation (f_{21}) was set to the ratio of aspartate to glutamate composition in the average mammalian protein (0.887, Voet and Voet, 1990).

The normalized sum of least squares error (NLSE) for this model ranged from 0.76 to 4.1 and averaged 1.97. The NLSE is the sum of least squares error from a weighted fit normalized by the number of data points. An NLSE less than one indicates that the results and the model fit within the one standard deviation of the data. The NLSE could be zero if the model perfectly fit the data. The NLSE was used to evaluate the feasibility of the various models. Seven models had an average NLSE of order one and were feasible based on the quality of the fit alone. Three models had an average NLSE more than an order of magnitude higher, and were clearly infeasible.

A model lacking these four biosynthesis and biodegradation fluxes (f_{21}, f_{22}, f_{29}, and f_{30}) was used to test their necessity. Rational for this model is based on three arguments: Nucleoside biosynthesis is mostly likely small because of the low concentration of formate in DME medium; formate is required for purine biosynthesis. Assuming that fatty acids and cholesterol are required predominantly for membrane formation, their synthetic rates would also be slow, because of the slow growth rate of MCF7 cells. The most ambiguous component is the rate of protein turnover, which varies from minutes to months depending on the protein (Dice and Goldberg, 1975; Voet and Voet, 1990), and could contribute a significant carbon flux (Portais et al., 1993; Sharfstein et al., 1994; Bonarius et al., 1996). While these assumptions fit many

hypotheses regarding cancer cell function, the average NLSE for this model was 34.0, almost twenty times the NLSE of the best model, indicating that at least protein turn over is a significant flux in MCF7 cells.

The observation that cerulenin treatment increases glutamate production implies that glutamine is consumed to provide precursors for biosynthesis. Blocking fatty acid synthesis would increase these precursor and glutamate pools resulting in an increased glutamate excretion. A model, contrasting the biosynthesis-inactive model, was tested that lacked the biodegradation fluxes (f_{22} and f_{30}) and contained two additional paths, a fatty acid degradation path (f_{24}) and a biosynthetic path originating from glyceraldehyde-3-phosphate (not shown in Fig. 5.18). This additional biosynthetic flux is a lumped pathway composed of *de novo* synthetic routes to serine, glycine, ribose, and pyrimidines. This model assumes that a significant fraction of the carbon consumed by growing cells is used for biosynthesis. However, this model was also infeasible because of its high NLSE of 18.2.

The flux results provide a reason for the high NLSE. The association factor for glutamate exchange (α_2) was forced to one for all six of the treatments, indicating that the transport of glutamate needed to exchange rapidly (more than 100 times the glycolytic flux) to supply unlabeled glutamine carbons into the mitochondria. Such a rate of membrane transport is highly improbable. Also, the fraction of isotope enrichment in the second and third carbons of glutamate is significantly less than in the fourth carbon. Together, these observations indicate that a "per-turn" dilution of isotope is occurring in the TCA cycle, i.e. an alternate flux of unlabeled carbon is entering the TCA cycle. Previously, both Portais et al. (1993) and Sharfstein et al. (1994) observed that the

31

catabolism of medium components was insufficient to explain the "per-turn" dilution and added a generic degradation flux to compensate for it.

The assumption that biomass exchange rates of aspartate and glutamate are related by a ratio of 0.887 was tested with a model that arbitrarily set this ratio to 1.5. There was no physical basis for this value; it was used to test the sensitivity of the results to the ratio. All of the resultant fluxes varied by less than 1%, except the four biosynthesis/biodegradation fluxes. Interestingly, the two pairs of fluxes averaged to the same value in the two models.

Constraining the biodegradation fluxes equal to the biosynthetic fluxes was an arbitrary assumption. The synthetic rate should be slightly larger than the degradation rate in growing cells. A model was tested that constrained the biodegradation fluxes to be equal (f_{22} and f_{30}) and left the two biosynthetic (f_{21} and f_{29}) fluxes independent. While this model had an average NLSE of 1.92 and appeared physiologically feasible, the results were unstable and dependent on the initial guesses for the independent fluxes. The full set of flux results for this model and the more constrained model are listed in appendix III. Even though this model was over-defined by four variables (16 measurements and 12 independent fluxes, i.e., no degrees of freedom), the biosynthetic fluxes were weakly dependent on the measured isotopomer fractions, casting doubt on the results of this model. For most of the treatments, the biosynthesis fluxes were between 100% and 120% of biodegradation fluxes indicating that constraining them to be equal was reasonable.

6. TCA Cycle Metabolite Channeling

The metabolic pathway model in Fig 5.18 contains two fluxes (f_{17} and f_{18}) from α-ketoglutarate to the lumped metabolite comprised of malate, oxaloacetate, and aspartate. Each of these fluxes representing one of the two rearrangements of α-ketoglutarate carbons possible in malate. Two of the TCA cycle intermediates, succinate and fumarate, are symmetric. If they were free to rotate in solution, the values of f_{17} and f_{18} would be equal because both orientations of malate would be possible. However, f_{17}, which maps the fifth carbon of α-ketoglutarate onto the first of malate, is greater than or equal to f_{18} for all of the treatments, indicating that it is the preferred orientation.

The preference of one orientation over the other can be explained by a supramolecular metabolon on the inner mitochondrial membrane (Srere, 1990) as described in chapter two. Estrogen affects the phosphorylation of metabolic enzymes (Cooper et al., 1983), which in turn induces complex formation (Mazurek et al., 1996). In control cells f_{17} was favored over f_{18} almost two to one. However, in estradiol treated cells the two paths are equal, indicating that estradiol disrupts the TCA cycle metabolon.

B. Conclusions

The flux results in Table 5.4 represent the first attempt to analyze metabolic fluxes in breast cancer cells and the first attempt to quantify the metabolic effects of estradiol. A novel solution method was developed that utilized isotopomer data, efficiently handled reversible reactions, and generated errors for the flux results. The method is capable of determining the intracellular metabolic fluxes in all types of cells, and can incorporate any hypothesized pathway model. The results in the previous section are the outcome of over 1200 stable runs of this method. The final, most appropriate

pathway model contained seven independent intracellular branches in addition to mitochondrial compartmentalization.

The advancements of a model that contains mitochondrial compartmentalization as well as a means to describe the reversibility of reactions enabled us to determine that the malate-aspartate shuttle is inactive in MCF7 cells. This result and the inactivity of intra-mitochondrial malic enzyme offer new insights into the metabolism of cancer cells. The inability of cancer cells to transport reducing equivalents into the mitochondria may be the long sought after explanation of the Warburg effect. From our results we hypothesize that the elevated NADH level in the cytosol increases mitochondrial uptake of glutamine and production of aspartate and citrate, two biosynthetic precursors. This hypothesis thus provides a link between aerobic glycolysis, glutaminolysis, and increased proliferation.

A few other traits of MCF7 breast cancer cells grown in DME medium and treated with 0.5 µM estradiol were identified. Estradiol stimulated many metabolic pathways including glycolysis, the pentose phosphate pathway, and glutaminolysis. The last two are noteworthy because they provide precursors for biosynthesis. By using cerulenin to inhibit fatty acid synthase, it was determined that this enzyme's demand for NADPH from does not affect the flux through the pentose phosphate pathway. By using oxamate to inhibit lactate dehydrogenase it was determined that its activity does not control the glycolytic rate or affect growth rate. A large biomass exchange flux, most likely protein turnover, was necessary to explain the observed isotopomer pattern. The observation of a preference for a single pattern of carbon rearrangement in TCA cycle metabolites supports the existence of a metabolon, or complex, of TCA cycle enzymes.

34

These results identified a few enzymes critical to cancer cell proliferation that are possible therapeutic targets. Reducing the elevated cytosolic NADH/NAD$^+$ ratio by slowing glycolysis may reduce the production of precursors by the mitochondria. A few excellent targets have recently been identified for this purpose. A phosphofructokinase-II isoenzyme was found to be over-expressed in cancer cells (Chesney et al., 1999). The product of this enzyme, fructose 1,6-bisphosphate stimulates glycolysis. Dang and Semenza (1999) identified a consensus binding-site for the carbohydrate-response element (ChoRE), the hypoxia-inducible growth factor (HIF-1), and the oncogene cMYC. These factors induce the expression of many glycolytic enzymes. Many cancer cells over-express hexokinase II, a membrane bound isoenzyme that increases glycolysis.

Directly inhibiting the mitochondrial consumption of glutamine may be another approach. Glutaminase deamidates glutamine to glutamate soon after it is consumed. The glutamate/aspartate anti-port is critical for the excretion of aspartate and probably the most significant route for glutamine carbons to enter the mitochondria. The consumption of glutamine and the action of pyruvate carboxylase are the two chief means by which biosynthetic precursors are produced. Any compound that can specifically target any of these enzymes in cancer cells would be excellent therapeutics.

Metabolic flux analysis is a holistic and integrative approach to investigating the characteristics of cancer cells. Many decades of study have shown that the mechanisms of cancer cell proliferation are highly multivariate and interdependent, and cannot be fully explained by reductive investigations of single pathways. Reductive investigations are essential for discovering the possible functions of intracellular pathways and enzymes. However, demonstrating that enzymes are capable of catalyzing specific

reactions or binding other proteins *ex vivo* does not prove that those functions occur within living cells. An integrative study that compares multiple functions and quantifies their effects, will determine which functions are predominant, and are therefore critical for survival and proliferation. Hopefully, as more integrative methods are employed and a better understanding of cancer cell proliferation is determined, improved treatments may soon be developed.

References

Braun S, Kalinowski HO, Berger S. 1996. 100 and More Basic NMR Experiments. New York: VCH.

Damadian R. 1981. NMR in medicine. Berlin: Springer-Verlag.

Degani H, Dejordy JO, Salomon Y. 1991. Stimulation of cAMP and Phosphomonoester Production By Melanotropin in Melanoma Cells - P-31 NMR Studies. *Proceedings of the National Academy of Sciences of the United States of America* **88**:1506-1510.

Freshney RI. 1994. Culture of Animal Cells. New York: Wiley-Liss.

Hwang SH. 1996. Growth and Metabolism of Human Breast Cancer Cells on Microcarriers. *Masters Thesis*. University of California at Berkeley.

Metz KR, Dunphy LK. 1996. Absolute Quantitation of Tissue Phospholipids Using P-31 Nmr Spectroscopy. *Journal of Lipid Research* **37**:2251-2265.

Portais JC, Schuster R, Merle M, Canioni P. 1993. Metabolic Flux Determination in C6 Glioma Cells Using Carbon-13 Distribution Upon [1-C-13]Glucose Incubation. *European Journal of Biochemistry* **217**:457-468.

Appendix B

Using Isotopomer Path Tracing to Quantify Metabolic Fluxes in Pathway Models Containing Reversible Reactions

Neil S. Forbes, Douglas S. Clark, and Harvey W. Blanch
Department of Chemical Engineering
University of California at Berkeley
Berkeley, CA 94720

Corresponding Author: Prof. Harvey W. Blanch
Department of Chemical Engineering
University of California at Berkeley
Ph: (510) 642 - 1387
Email: blanch@socrates.berkeley.edu

Running Title: Quantifying Metabolic Fluxes with Isotopomer Path Tracing

Summary

As a more complete picture of the genetic and enzymatic composition of cells becomes apparent, there is a growing need to describe how these cellular regulatory elements interact with the cellular environment to affect cell physiology. One means for describing intracellular regulatory mechanisms is concurrent measurement of multiple metabolic pathways and their interactions by metabolic flux analysis. Flux of carbon through a metabolic pathway responds to all cellular regulatory systems, including changes in enzyme and substrate concentrations, enzyme activation or inhibition, and ultimately genetic control. The extent to which metabolic flux analysis can describe cellular physiology depends on the number of pathways in the model and the quality of the data. Intracellular information is obtainable from isotopic tracer experiments, the most extensive being the determination of the isotopomer distribution, or specific labeling pattern, of intra-cellular metabolites. In this work we present a rapid and novel solution method that determines the flux of carbon through complex pathway models using isotopomer data. This time-consuming problem was solved with the introduction of *isotopomer path tracing*, which drastically reduces the number of isotopomer variables to the number of isotopomers observed experimentally. We propose a partitioned solution method that takes advantage of the nearly linear relationship between fluxes and isotopomers. Whereas the stoichiometric matrix and the *isotopomer matrix* are invertible, simulated annealing and the Newton-Raphson method are used for the non-linear components. Reversible reactions are described by a new parameter, the *association factor*, which scales hyperbolically with the rate of metabolite exchange. Automating the solution method enables numerous models to be generated and compared thus enhancing

the accuracy of results. A simplified example that contains all of the complexities of a comprehensive pathway model is presented.

I. <u>Introduction</u>

In the past decades much has been learned about intracellular regulatory mechanisms. These mechanisms have been mainly deduced from reductive experiments focused on single metabolic pathways. However, a more complete understanding requires concurrent analysis of multiple pathways and a description of their interactions. These interactions may be quantified using metabolic flux analysis, which determines carbon flow through the pathways of primary and secondary metabolism. A *metabolic flux* is the rate of product formation per cell per time in a series of enzyme-catalyzed reactions. This activity is the response to all cellular regulatory systems, including changes in enzyme and substrate concentration, allosteric activation or inhibition, and ultimately genetic control. Flux analysis is thus the first step in providing a comprehensive mechanistic description of cellular behavior and function.

Describing cellular regulation using metabolic models with few intracellular pathways is difficult. It is therefore desirable to determine as many intracellular fluxes as possible. Isotopomer tracer measurements provide a unique route for quantifying intracellular fluxes and discriminating between proposed pathway models. An *isotopomer* is a metabolite with a specific ^{13}C labeling pattern. A metabolite with n carbons thus has 2^n isotopomers (Schmidt et al., 1997).

Recently, several elegant approaches have been proposed for converting isotopomer data into a set of fluxes (Schmidt et al., 1999a; Wiechert et al., 1999). In the present work we introduce two concepts that drastically increase the speed of this conversion by analyzing many of the complexities of isotope flow prior to iterative simulation. *Isotopomer path tracing* and a new parameter, the *association factor*,

generate a direct mapping from isotopomer measurements to metabolic fluxes, thereby dramatically reducing the number of variables in the system.

A. Pathway Models

The first step in the metabolic flux analysis is the development of a biochemical pathway model. Pathways are typically selected from the set of known cellular reactions based on their significance to carbon and isotope flow (Forbes et al. 2000).

Figures 1 and 2

Figure 1 is a model generally applicable to transformed mammalian cells. The abbreviated model in Fig. 2 will be used as an example of a typical pathway structure. It contains a simplified tricarboxylic acid (TCA) cycle (f_5, f_6), and an exchange flux (f_8). The most significant difference between the two models is the number of carbons per metabolite. The pseudo-metabolites in Fig. 2 have half the carbons of their corresponding metabolites in Fig. 1.

B. Measurements: Extracellular Fluxes and Isotope Labeling Patterns

For illustrative purposes, we consider a hypothetical experiment on a mammalian cell line having the metabolic pathways assumed in Fig. 2. This example was chosen to provide a basis for the discussion of methods detailed in this paper. These methods can, without modification, be applied to continuous, perfusion, or batch cultures of prokaryotic or eukaryotic cells, with NMR and/or mass spectrometry-based measurements.

The two types of measurements necessary for flux determination are extracellular fluxes and isotope fractions. For our example, let us assume that the concentrations of pseudo-metabolites **G**, **S**, and **Q** are measured as a function of time. From these measurements the extracellular fluxes f_1, f_2, and f_9 can be calculated. These extracellular

fluxes form part of the vector, $\underline{\mathbf{d}}^{\text{meas}}$, which contains all measured variables. For example, we assume the values given in Eq. (1) were obtained:

$$\underline{\mathbf{d}}^{\text{meas,extra}} = \{f_1, f_2, f_9\} = \{1, 0.3, 0.4\} \tag{1}$$

These values were normalized by f_1 and are therefore dimensionless.

We further assume that during the course of the experiment the cultures were fed $1\text{-}^{13}\text{C}$ **G**. After reaching steady state, the cytoplasm of the culture was extracted. A ^{13}C-NMR spectrum of the extracts contained peaks for the carbon of metabolite **A** and the first and second carbons of metabolite **E**. By integrating these spectral peaks, the isotopomer fractions, A_0, A_1, E_0, E_1, E_2, and E_3 could be quantified. An *isotopomer fraction* is the ratio of the concentration of a specific isotopomer to the concentration of that metabolite. The isotopomer fractions are numbered according to the convention established by Schmidt et al. 1997 and as given in Appendix A. These fractions form the second part of the vector of measured variables, $\underline{\mathbf{d}}^{\text{meas,isotop}}$. Here we assume

$$\underline{\mathbf{d}}^{\text{meas,isotop}} = \{A_0, A_1, E_0, E_1, E_2, E_3\} = \{0.35, 0.65, 0.55, 0.2, 0.09, 0.16\} \tag{2}$$

The measurement vector concatenates the two normalized vectors: $\underline{\mathbf{d}}^{\text{meas}} = |\underline{\mathbf{d}}^{\text{meas,extra}} | \underline{\mathbf{d}}^{\text{meas,isotop}} |$. The overall goal of flux analysis is then the determination of the complete set of fluxes, $\underline{\mathbf{f}}$, from $\underline{\mathbf{d}}^{\text{meas}}$ and the pathway model. The corresponding standard deviations, $\underline{\sigma}$, of the measurements in the vector of measured variables are assumed in this example to be

$$\underline{\sigma} = \{0.05, 0.02, 0.02, 0.02, 0.02, 0.03, 0.01, 0.005, 0.01) \tag{3}$$

C. The Stoichiometric Matrix

Expressed in matrix form, the mass balances around the metabolites in a pathway model are

$$\underline{\underline{A}} \cdot \underline{f} = \underline{b} \tag{4}$$

Here $\underline{\underline{A}}$ is the stoichiometric matrix, $\underline{f}$ is the vector of all fluxes, and $\underline{b}$ is the constraint vector. The stoichiometric matrix, $\underline{\underline{A}}$, is the concatenation of the intracellular- and extracellular-metabolite stoichiometric matrices. For Fig. 2., $\underline{\underline{A}}$ is

$$\underline{\underline{A}} = \begin{bmatrix} \underline{\underline{A}}^{intra} \\ \hline \underline{\underline{A}}^{extra} \end{bmatrix} = \begin{array}{c} \begin{array}{cccccccccc} f_1 & f_2 & f_3 & f_4 & f_5 & f_6 & f_7 & f_8 & f_9 & f_{10} \end{array} \\ \left[\begin{array}{cccccccccc} 1 & 1 & -1 & -1 & 0 & 0 & 0 & 0 & 0 & 0 \\ 0 & 0 & 0 & 1 & -1 & 0 & 1 & 0 & 0 & 0 \\ 0 & 0 & 0 & 0 & 1 & -1 & -1 & 0 & 0 & 0 \\ 0 & 0 & 0 & 0 & -1 & 1 & 0 & 1 & 0 & 0 \\ 0 & 0 & 0 & 0 & 0 & 0 & 0 & -1 & 1 & -1 \\ \hline -1 & 0 & 0 & 0 & 0 & 0 & 0 & 0 & 0 & 0 \\ 0 & -1 & 0 & 0 & 0 & 0 & 0 & 0 & 0 & 0 \\ 0 & 0 & 0 & 0 & 0 & 0 & 0 & 0 & -1 & 0 \end{array} \right] \end{array} \begin{array}{c} F \\ A \\ C \\ O \\ E \\ G \\ S \\ Q \end{array} \tag{5}$$

The stoichiometric matrix exactly describes every flux and is therefore synonymous with the pathway model (Figs. 1 and 2). The constraint vector, $\underline{b}$, is the concatenation of a zero vector and the vector of measured extracellular fluxes: $\underline{b} = [\ \varnothing \mid \underline{d}^{meas,extra}\ ]$.

In this example, $\underline{\underline{A}}$ is twice rank deficient. It could be rendered square by defining two additional constraints (Goel et al., 1993; Jorgensen, 1995; Vallino and Stephanopoulos 1992). However when investigating cellular regulation it is generally desirable to minimize the number of assumptions. In our analysis, additional constraints were avoided, and the complete set of fluxes determined, through the use of isotope balances.

II. Isotope Flux Balances and Paths

A steady state isotope balance can be written around each carbon atom of a pathway model:

$$\sum \lambda_{out} = \sum \lambda_{in} \tag{6}$$

where λ_{out} and λ_{in} designate isotope paths out and in of a given carbon. An isotope path represents a flux of ^{13}C from one carbon to another. In other words, the value of λ_i is the flux of isotope through the path and has the units: atoms of ^{13}C per cell per time. To generate these isotope balances, the isotopomer paths must first be identified and the functions describing them determined. This is the primary function of isotopomer path tracing.

Only a small fraction of the nearly 1000 isotopomers in a pathway model (Fig. 1) can be measured. Here we introduce the concept of isotopomer path tracing, which only identifies paths between *observable* isotopomers, many of which are separated by *non-adjacent* isotope paths. Both an adjacent, λ_1, and a non-adjacent, λ_2 isotope path are highlighted in Fig. 3.

Figure 3

The flux through the adjacent path, λ_1, from the first carbon of **G** to the first carbon of **F** is defined (Forbes et al. 2000) as

$$\lambda_1 = \lambda_{G1 \to F1} = \frac{f_1}{v_{G1}} G1 = f_1 \cdot G1 \tag{7}$$

The subscript G1→F1, describes the initial and final carbons of the isotope path. G1 is the fractional enrichment by ^{13}C of the first carbon of **G**. The stoichiometric ratio, v_{G1}, is defined as moles of products formed divided by moles of reactant consumed (equal to one for most paths). This and other isotope path examples in this paper are based on fractional enrichments for ease of explanation. In all cases, the exact same structure would apply if the examples were based instead on isotopomer fractions.

When describing the non-adjacent isotope path in Fig. 3, λ_2, F1 is assumed to be un-measurable. A function for λ_2 must therefore be determined that is independent of F1. The adjacent isotope balances around the first carbons of metabolites **F** and **X** are

$$\text{F1:} \quad \text{F1 } (f_3 + f_4) = \text{G1 } f_1 \tag{8}$$

$$\text{X1:} \quad \text{X1 } (f_5 + f_6) = \text{F1 } f_2 \tag{9}$$

By combining Eqs. (8) and (9) and eliminating F1, the isotope balance around X1 yields the isotope flux, λ_2:

$$\text{X1 } \left(f_5 + f_6\right) = \left(\frac{f_4}{f_3 + f_4}\right) \text{G1 } f_1 = \lambda_2 \tag{10}$$

This isotope flux relationship between G1 and X1 is non-linear in f_4, and thus cannot be incorporated into the stoichiometric matrix. However, if F1 and every isotopomer in the pathway model are measured, the linear Eq. (8) could be incorporated into **A**.

III. <u>The Solution Method</u>

The non-linearity of Eq. (10) and the inability to obtain an analytical relation between isotopomer fractions and metabolite fluxes dictates the use of an iterative solution method. While analytical solutions have been obtained for models with fewer pathways than illustrated in Fig. 1 (Klapa et al., 1999; Sharfstein et al., 1994), such solutions cannot be found for models with unlabeled carbon sources or more than two branched pathways.

A. Hierarchy

If the calculation of fluxes were to be treated as a single large non-linear problem, all of the nearly 1000 fluxes and isotopomers would be variables. Current commercially available modeling software becomes intractable in 1000-dimension space. We reduce

the large scale of this problem with the two-step solution method depicted by the flow chart in Fig. 4. Isotopomer path tracing reduces the number of variables in the system, which enables a solution to be found and reduces the simulation time to minutes. Tracing only needs to be performed once for each pathway model and typically takes only a few seconds.

Figure 4.

The inputs to the solution method in Fig. 4 are highlighted, and include the stoichiometric matrix, $\underline{\mathbf{A}}$, the experimental measurements, $\underline{\mathbf{d}}^{meas}$, the set of atom mapping matrices (**AMM**s, Zupke and Stephanopoulos, 1994), initial guesses for the independent fluxes, $\underline{\mathbf{q}}_0$, and the isotopomer input vector, $\underline{\eta}$. The **AMM**s describe the conversion of atoms of a substrate to the atoms of a product by a given reaction. They are constants that must be defined for each reaction *a priori*. The quantities $\underline{\mathbf{q}}_0$ and $\underline{\eta}$ will be described in detail later in this section.

Because the equations employed in flux analysis are very nearly linear, it is advantageous to group the linear and non-linear components of the iterative simulation (the right box in Fig. 4) into a nested hierarchy. The linear components, the stoichiometric and isotopomer matrices (the white box of Fig. 4), can be quickly inverted and have unique solutions. The non-linear components are solved using algorithms specific to their forms. Simulated annealing is described in more detail later in this section.

The Newton-Raphson multivariate root-finding method (Press et al. 1992) is used to determine the *isotopomer vector*, $\underline{\omega}$, which is a column vector of isotopomers. It is composed of a series of *isotopomer fraction vectors,* $\underline{\mathbf{E}}$, $\underline{\mathbf{A}}$, $\underline{\mathbf{O}}$, and $\underline{\mathbf{C}}$, which contain all

isotopomer fractions for the metabolites **E**, **A**, **O**, and **C** in Fig. 2. The isotopomer vector, $\underline{\omega}$, cannot be entirely determined by matrix inversion because $\underline{C}$ is non-linearly dependent on $\underline{A}$ and $\underline{O}$:

$$\underline{C} = \underline{IMM}_{A \rightarrow C} \cdot \underline{A} * \underline{IMM}_{O \rightarrow C} \cdot \underline{O} \tag{11}$$

The "*" symbol indicates element-wise vector multiplication. The *isotopomer-mapping matrices* $\underline{IMM}_{A \rightarrow C}$ and $\underline{IMM}_{O \rightarrow C}$ are as defined by Schmidt et al. 1997. This implementation of the Newton-Raphson method is described in section VI.

B. Independent Fluxes

The stoichiometric matrix, $\underline{A}$ must be rendered square before it can be inverted in step two of Fig. 4. The rank deficiencies of $\underline{A}$ correspond to branches in the pathway model. A *branch metabolite* has multiple out-fluxes, one of which is arbitrarily designated *independent* (or free, Wiechert and de Graaf 1997). The two independent fluxes in Fig. 2 are f_3 and f_{10}, which originate from branch metabolites, **F** and **E**, respectively. Each independent flux corresponds to a row of the independent flux matrix, $\underline{A}^{indep}$, which is concatenated to $\underline{A}$, i.e., $\underline{A} = [\underline{A}^{intra} | \underline{A}^{extra} | \underline{A}^{indep}]$. For Fig. 2., $\underline{A}^{indep}$, is

$$\underline{A}^{indep} = \begin{array}{c} \begin{matrix} f_1 & f_2 & f_3 & f_4 & f_5 & f_6 & f_7 & f_8 & f_9 & f_{10} \end{matrix} \\ \begin{bmatrix} 0 & 0 & 1 & 0 & 0 & 0 & 0 & 0 & 0 & 0 \\ 0 & 0 & 0 & 0 & 0 & 0 & 0 & 0 & 0 & 1 \end{bmatrix} \end{array} \begin{array}{c} f_3 \\ f_{10} \end{array} \tag{12}$$

Inverting $\underline{A}$ enables calculation of a working flux vector, $\underline{f}^{calc}$, from a vector of guesses, $\underline{q}$. The constraint vector in Eq. (4) is now redefined as $\underline{b} = [\varnothing | \underline{q}^{extra} | \underline{q}^{indep}]$, where $\underline{q}$ contains guesses for the extracellular and independent fluxes. The most reasonable initial guesses for the extracellular fluxes are the measured values. However, estimates must be made for the independent fluxes. In the present example, the initial

guess, $\underline{g}_0$, is assumed to be $\{1, 0.3, 0.4, 0.5, 0.1\}$, which produces $\underline{f}^{calc} = \underline{A}^{-1} \cdot \underline{b} = \{1, 0.3,$ $0.5, 0.8, 1.1, 0.8, 0.3, 0.3, 0.4, 0.1\}$ for the first iteration of the simulation.

C. The Isotopomer Matrix, (Θ)

Steps three through eight in Fig. 4 calculate the vector of measured isotopomers, $\underline{d}^{calc,isotop}$ from $\underline{f}^{calc}$ using the inverse of the isotopomer matrix, $\underline{\Theta}$. The elements of $\underline{\Theta}$ are functions of only fluxes and are derived from the isotopomer flux balances, e.g., Eq. (10). While these balances are not linear in fluxes, they are linear with respect to isotopomer fractions. Grouping all of the flux terms together as coefficients enables the balances to be written in matrix form:

$$\underline{\Theta} \cdot \underline{\omega} = \underline{\eta} \tag{13}$$

The isotopomer vector, $\underline{\omega}$, contains all isotopomers detected in the experiment ($\underline{d}^{calc,isotop}$), the input isotopomers, and additional isotopomers to assist the numerical analysis. For the example experiment it has 21 elements and is $\{G_1, S_0, Q_0, \underline{E}, \underline{A}, \underline{O}, \underline{C}\}$. The non-zero elements of the isotopomer input vector, $\underline{\eta}$, are the isotopomer fractions of the nutrients fed to the cells. The only non-zero elements of $\underline{\eta}$ in the example are the first three, G_1, S_0 and Q_0. Because the feed contained completely labeled **G** and completely *un*-labeled **S** and **Q**, these three elements are all equal to 1.0.

The isotopomer matrix is a sparse matrix whose non-zero elements, $\theta_{i,j}$, correspond to the isotope paths from source isotopomers, ω_i, to target isotopomers, ω_j. For the example experiment, $\underline{\Theta}$ is

$$
\begin{bmatrix}
1 \\
 & 1 \\
 & & 1 \\
 & & F_1 & -\beta_E \\
 & & & & -\beta_E \\
 & & & & & -\beta_E \\
 & & & & & & -\beta_E \\
 & F_3 & & & & & & -\beta_A \\
F_4 & & & & & & & & -\beta_A \\
 & F_5 & & & & & & & & -\beta_O \\
 & & & & & & & & & & -\beta_O \\
 & & & & & & & & & & & -\beta_O \\
 & & & & & & & & & & & & -\beta_O
\end{bmatrix}
\tag{14}
$$

where F_i are functions of fluxes given by

$$
\begin{aligned}
F_1 &= \frac{\beta_E^{net}}{\beta_E^{net} + \alpha_{EO}} f_9 & F_4 &= \frac{f_4}{\beta_F} f_1 \\[2mm]
F_2 &= \frac{\beta_E^{net} \cdot \alpha_{EO}^{*}}{\beta_O^{net} + \alpha_{OE}} f_6 & F_5 &= \frac{f_8^{net} + \alpha_{EO}}{\beta_E^{net} + \alpha_{EO}} f_9 \\[2mm]
F_3 &= \frac{f_4}{\beta_F} f_2 & F_6 &= \frac{\beta_O^{net}}{\beta_O^{net} + \alpha_{OE}} f_6
\end{aligned}
\tag{15}
$$

A metabolite throughput, β_X, is the total flow through a metabolite pool and is a summation of fluxes. An association factor, α, describes the reversibility of an exchange reaction. Both of these parameters and the determination of the functions in Eqs. (14) and (15) are described in more detail in Sections IV and V.

D. Simulated Annealing

The remaining steps of the flow chart in Fig. 4 are based on the simulated annealing method described by Schmidt et al., 1999b. In summary, the method begins with making an initial guess for the independent fluxes, $\underline{q}_0$. This guess forms the constraint vector, $\underline{b}$, from which the entire calculated flux vector is determined. The

calculated isotope pattern, $\underline{\mathbf{d}}^{calc,isotop}$, corresponding to the arbitrary flux values is found using the isotopomer matrix, $\underline{\Theta}$, and the Newton-Raphson method. The weighted least squares error (LSE) is the difference between the measured and calculated vectors, $\underline{\mathbf{d}}^{meas}$ and $\underline{\mathbf{d}}^{calc}$ divided by the vector of standard deviations, $\underline{\sigma}$. Finally, acceptable guessed independent fluxes, $\underline{\mathbf{q}}$, are recorded and a new vector is generated. The simulation concludes after N iterations.

Simulated annealing was used to "escape" local minima and plateaus and approach the global minimum (Schmidt et al., 1999b, Press et al., 1992). Rather than retaining parameter sets that reduce the least-square error, a parameter set is retained if the error is smaller than the previous lowest error with the addition of a predetermined dead band. The value of this dead band is reduced from an initial value to zero after a specified number of iterations. This method allows the solver to approach the solution more slowly, increasing the likelihood that it will find the global minimum.

IV. Tracing Isotopomer Paths

Four major obstacles are encountered in determining $\underline{\Theta}$: the unmanageably large number of isotopomers, and the presence of problematic pathways involving splitting, joining, and exchange reactions. The large number of isotopomers is handled by isotopomer path tracing, and the three problematic pathway types are addressed in the next sections.

A. Automation

Many possible pathway models can be created from the set of all known metabolic pathways (Forbes et al. 2000). Those that predict physiologically unrealizable fluxes from the measurements are eliminated, thus increasing the confidence in the

remaining models. This approach requires that many models be created, including the corresponding $\underline{\mathbf{A}}$ and $\underline{\Theta}$ matrices.

Because determining $\underline{\Theta}$ is algebraically complex, it is time consuming to manually generate $\underline{\Theta}$ for each model. Therefore, a robust computer algorithm was developed that automatically determines $\underline{\Theta}$. *Visual Basic* code was used to implement the algorithm because of its easy interface with *Excel* spreadsheets. These sheets were used to store the large input and output matrices. The code is available from the authors upon request.

B. Superposition

The superposition concept facilitates the creation of simpler algebraic forms of the isotope paths. As shown in Fig. 5, the isotope path from G1 to C2 in Fig. 2 passes through C1.

Figure 5.

While this path is not very long or complicated, there are paths between the observable isotopomers in Fig. 1 that, due to cyclic pathways, are very long or infinite. By superposition, these long or infinite isotope paths can be replaced by an amalgam of smaller paths if the intermediary fractional enrichments are known. The longer path λ_1 need not be traced if both shorter paths λ_2 and λ_3 are. By including isotope paths from intermediate observable isotopomers, the tracing process is thus simplified.

C. Metabolite Throughput

In Fig. 3 and its corresponding non-adjacent flux balance, Eq. (10), X1 is dependent on only four quantities: the fractional enrichment of the "source" metabolite,

G1; the "source outlet flux," f_1; the dilution caused by the branch, $f_4/(f_3+f_4)$; and the metabolite *throughput*, (f_5+f_6). This throughput of **X** is denoted as β_X.

When generating isotopomer balances, Eq. (6), the sum of isotopomer fluxes *out* of an isotopomer pool, $\Sigma\lambda_{out}$, is simply $Xj \cdot \beta_X$, where Xj is the fractional enrichment of the jth carbon of **X**. Because $\Sigma\lambda_{out}$ is independent of other isotopomer fractions, it is only necessary to determine the sum of the isotopomer paths *into* an isotopomer pool, $\Sigma\lambda_{in}$, to close the balances.

D. Pathway Notation

An explicit equation for the flux through a non-adjacent branched isotopomer path (Fig. 3) has already been derived in Eq. (10). A generalized form of Eq. (10), applicable to all non-adjacent paths is

$$\lambda_{Oi\to Xj} = \left[\prod_k^K \frac{f_k^{outlet}}{\beta_k}\right] Oi \cdot f_{source}^{outlet} \qquad (16)$$

where $\lambda_{Oi\to Xj}$ is the isotope path from the source carbon of **O** to the target carbon of **X** and Oi is the fractional enrichment of the ith carbon of **O**. The fluxes, f_k^{outlet} and f_{source}^{outlet}, are the outlet flux from a branch metabolite and the source metabolite, respectively. In Eq. (10) the branch outlet flux is f_4 and the source outlet flux is f_1. Branches in isotopomer paths cause the flow of isotope to diminish in proportion to *dilution fractions*, (f_k^{outlet} / β_k), where β_k is the throughput of the kth branch metabolite. There are K branch metabolites in the isotope path $\lambda_{Oi\to Xj}$. The product operator accounts for isotope paths with multiple branches.

E. The Tracing Algorithm

A flowchart for the tracing algorithm is shown in Fig 6.

Figure 6.

This algorithm identifies all isotopomer paths that produce an observable isotopomer. There are two sections in the algorithm: back-steps from the observable isotopomer, and the returning forward-steps towards it. Stepping backwards identifies legitimate isotopomer paths and stepping forwards ensures that all possible paths are traced.

1. Stepping Back: the Basic Iterative Steps of Isotopomer Path Tracing

Isotopomer paths are traced in the opposite direction to carbon flow, because only the isotopomer paths producing an observable isotopomer, $\Sigma\lambda_{in}$, must be found. In the process of stepping along isotopomer paths, four types of metabolites are encountered. A metabolite can be the site of a branch, a merge, neither, or both. A *merge metabolite* is similar to a branch metabolite in that it has multiple in-fluxes.

The three segments of a back-step are shown in Fig. 7.

Figure 7.

Step 1: One of the in-fluxes to the target metabolite is chosen. In Fig. 7, A_1 has two in-fluxes, f_4 and f_7. **Step 2**: The source of the flux is determined. **Step 3**: The isotopomer of the source metabolite is computed using the AMM corresponding to the flux as described in appendix A. In this case the source is F_1.

A path is terminated if the source metabolite is an observable isotopomer or an extracellular metabolite. Paths are recorded as terms in the elements of $\underline{\Theta}$ if they terminate in observable isotopomers or acceptable metabolites. An acceptable extracellular metabolite is either unlabeled or one of the supplied isotopically labeled nutrients. Each term in the elements of $\underline{\Theta}$ contains the components of Eq.(16): the source metabolite, the source outlet flux, and the dilution fraction for each branch metabolite. In the case of multiple paths between the same two isotopomers, the terms are simply added.

2. Stepping Forward: Accounting for Merge Metabolites and Splitting Fluxes

When stepping back past splitting fluxes, as in Fig. 8, it is impossible to conclusively determine the isotopomer of the source.

Figure 8.

The number of possible isotopomers of the source is equal to the number of possible isotopomers of the unknown product: 2^n, where n is the number of carbons of **X**.

The algorithm systematically cycles through every in-flux of a merge metabolite and every unknown isotopomer of a splitting flux in order to trace every path. During the process of tracing back from splitting fluxes, many impossible paths are investigated; however, they are not recorded.

3. Quasi-Observable Isotopomers

Unmeasured *quasi-observable* isotopomers are added to $\underline{\omega}$ to prevent the tracing algorithm from becoming ensnared in infinite loops. They interrupt cyclic flux pathways and trigger artificial termination of infinite isotopomer paths. The cost of their inclusion is an increase in the size of the isotopomer matrix and a subsequent increase in computation time.

The isotopomer fractions of the product of a joining reaction (**C** in Figs. 2 and 9) are dependent on the fractions of both sources (**A** and **O**). There are as many paths forming **C** as combinations of paths forming **A** and **O**. If, as in Fig. 9, there are a paths that produce A_1 and o paths that produce O_2, there are $a \cdot o$ paths that produce C_5.

Figure 9.

Both sources of joining fluxes are designated quasi-observables to avoid the computational problem of systemically intertwining all $a \cdot o$ paths. Conveniently, citrate

synthase, f_{14}, is the only joining reaction in Fig. 1. Designating oxaloacetate (OAA) as quasi-observable handles both the citrate synthase joining flux and the TCA cycle.

4. Tracing Example

As an example, we shall trace the isotopomer paths producing A_1 in Fig. 2, ignoring the return of label via f_7 for simplicity. In this simplified case, the only in-flux to **A** is f_4, which splits off two carbons. Therefore, f_4 has four "other" metabolite isotopomers. The first one traced is the 0th. Using the f_4 AMM, the first source isotopomer of f_4 is F_1. Next, one of the two in-fluxes into the merge metabolite **F** was selected. The first one is f_1, whose source is G_1. Because this was the feed metabolite, this path was recorded. The source is G_1, the source outlet flux is f_1, and the dilution fraction for the one branch at **F** is f_4/β_F.

Tracing forward, **F** is incomplete. The next in-flux to **F** is f_2, whose source is S_1. **S** is an extracellular metabolite, so the path is terminated. However, the path is not recorded because **S** is an unlabeled feed. Only a path terminating with S_0 would be recorded. Now **F** is complete, and the algorithm steps forward to f_4, which is incomplete. The algorithm traces back using the next isotopomer of the split product, the 1st. Two paths will trace from here terminating in G_3 and S_3, neither of which will be recorded. In the same manner, none of the paths from the two other split product isotopomers (2 and 3) of f_4 will be recorded.

In this simple example, the algorithm investigated eight pathways and recorded one. In contrast, automated tracing found 400-500 acceptable paths from the 10,000 investigated for the sample model in Fig. 1.

V. Accounting for Exchange Fluxes: The Association Factor

Tracing cannot account for exchange reactions and recursive loops. While adding quasi-observable isotopomers enables potentially infinite loops to be traced, this approach will not work for exchange fluxes.

Including exchange fluxes in a pathway model increases the accuracy of flux results and provides a more detailed description of cell physiology (Forbes et al. 2000; Weichert and de Graaf, 1997] Inexplicable isotope losses from net flux models can be accounted for by the inclusion of exchange fluxes. For example, the often-observed dilution of isotope in mitochondria (Portais et al., 1993; Sharfstein et al., 1994) can be explained by an exchange flux across the mitochondria membrane (Forbes et al. 2000).

A. Effects Of Exchange Fluxes on Isotopomer Paths

In Fig. 10, the exchange flux (f_8) affects the isotope pattern of metabolite **E** in the $\lambda_{Q1 \rightarrow P1}$ isotopomer path.

Figure 10.

If the exchange flux between two metabolites, **E** and **O**, is rapid, the isotopomer patterns of the two will be similar. However, if the exchange is slow the two metabolites will have more distinct patterns. In this section we will introduce a new parameter, the *association factor*, to describe the similarity of these two isotopomer pools.

1. Isotope Balances Based on Unidirectional Fluxes

Adjacent isotope balances around the first carbons of **E**, **O**, and **P** in Fig. 10 were combined to eliminate E1 and O1 in the isotope balance around P1:

$$\beta_P \cdot P1 = \left(\frac{f_{10}}{\beta_E - \frac{f_8^{\leftarrow} \cdot f_8^{\rightarrow}}{\beta_O}} \right) Q1 \cdot f_9 \tag{17}$$

56

The right hand side of Eq. (17) is $\lambda_{Q1 \to P1}$. The forward and backward unidirectional fluxes, $f_8^{\to}$ and $f_8^{\leftarrow}$, together describe the exchange flux, f_8. Because the net direction of the exchange flux is designated *a priori* (Weichert and de Graaf, 1997), the forward flux, $f_8^{\to}$, is defined such that it is greater than $f_8^{\leftarrow}$. The net flux is

$$f_8^{net} = f_8^{\to} - f_8^{\leftarrow} \tag{18}$$

The backward flux, $f_8^{\leftarrow}$, is equivalent to the exchange flux, v^{xch}, of Wiechert and de Graaf, 1997.

Equation (17) cannot be used in the tracing framework because it is dependent on the *unbounded* fluxes, $f_8^{\leftarrow}$ and $f_8^{\to}$, and throughputs, β_E, and β_O. Using unidirectional fluxes to describe an exchange flux can cause stiffness in the simulation because the fluxes approach infinity as the exchange becomes rapid (Wiechert and de Graff, 1997; Schmidt et al., 1999). Additionally, an exchange flux that is described by unidirectional fluxes will cause infinite looping in the tracing algorithm. Therefore another form of Eq. (17) is needed that is based on bounded terms and prevents the tracer from infinitely cycling.

2. *Effects of the Bounded Terms*

Bounded net-based throughputs are defined in the same manner as the net flux, Eq. (18); the backward flux is subtracted from the unbounded throughput:

$$\beta_E^{net} = \beta_E - f_8^{\leftarrow} \qquad\qquad \beta_O^{net} = \beta_O - f_8^{\leftarrow} \tag{19}$$

Figure 11 is a plot of the denominator of the dilution fraction in Eq. (17), $\beta_E - (f_8^{\leftarrow} \cdot f_8^{\to})/\beta_O$, as a function of $f_8^{\leftarrow}$. Each series has different values for β_O^{net} and f_8^{net}. The net throughput of **E**, β_E^{net} was held constant.

Figure 11.

When $f_8^{\leftarrow}$ is small, the exchange approaches unidirectionality, the denominator approaches β_E^{net}, and Eq. (17) approaches the form of Eq. (16). However, even at very large values of $f_8^{\leftarrow}$, when the exchange is rapid, the denominator remains bounded and the effect of the dilution fraction on the isotope path is finite. When $f_8^{\leftarrow}$ is large, the denominator approaches $\beta_E^{net} + (\beta_O^{net} - f_8^{net})$, which contains only net-based terms.

In Fig. 10, $\beta_O^{net} - f_8^{net} = f_6$. This is the flux of unlabeled carbon into **O** and is the maximum amount of isotope removed by the exchange. It defines the maximum dilution the exchange flux can exert on the isotope path. As $(\beta_O^{net} - f_8^{net})$ increases, the dilution fraction decreases. This is shown by the shift from the middle to the upper curve on Fig. 11.

The net throughput of **O**, β_O^{net}, has a dampening effect on the isotope path. The greater β_O^{net}, the greater $f_8^{\leftarrow}$ has to be for the exchange flux to affect the isotope path. This small effect is demonstrated by the shift from the middle to the lower curve in Fig. 11. β_O^{net} is increased from 2 to 5, while $(\beta_O^{net} - f_8^{net})$ is maintained constant.

3. Definition of the Association Factor

Equation (17) can be simplified by the inclusion of the net-based fluxes and throughputs, and a new parameter, α_{EO}, the association factor:

$$\beta_P \cdot P1 = \left(\frac{f_{10}}{\beta_E^{net} + \alpha_{EO}} \right) Q1 \cdot f_9 \qquad (20)$$

$$\alpha_{EO} = \frac{f_8^{\leftarrow}}{\beta_O} \left(\beta_O^{net} - f_8^{net} \right) \qquad (21)$$

Equation (20) has the same form as Eq. (16) with the addition of the single α_{EO} term. The numerator is the outlet branch flux, f_k^{outlet}, and the denominator is a modified throughput.

Dividing Eq. (21) by $(\beta_O^{net} - f_8^{net})$ gives the *normalized association factor*.

$$\alpha_{EO}^* = \frac{\alpha_{EO}}{\beta_O^{net} - f_8^{net}} = \frac{f_8^{\leftarrow}}{\beta_O} \qquad (22)$$

The normalized association factor scales from 0 to 1 as the exchange reaction ranges from unidirectional to rapidly exchanging. α_{EO}^* could also be written as

$$\alpha_{EO}^* = \frac{f_8^{\leftarrow}}{\beta_O^{net} + f_8^{\leftarrow}} \qquad (23)$$

Equation (23) is a hyperbolic function and is similar to the compacted exchange flux of Weichert and de Graaf, 1997: $v^{chx[0,1]} = v^{chx}/(1 + v^{chx})$. The advantage of the association factor notation is that each association factor is scaled appropriately for its reaction and location in the network. This allows the α notation to be incorporated into the tracing algorithm.

B. Incorporating the Association Factor into the Isotopomer Tracing Algorithm

1. Net Direction

Besides Fig. 10, there are other orientations the exchange reaction can have with respect to an isotopomer path. The exchange flux in Fig. 12 is embedded in the isotopomer path rather than being adjacent to it. For illustrative purposes, the size of molecules and the presence of isotope are different from Fig. 2.

Figure 12.

Because the net direction of the exchange reaction was designated *a priori*, it can have two possible orientations with respect to the isotope path. In scheme **I** the net direction is the same as that of the isotopomer path, whereas in scheme **II** it is opposite. The most significant difference between the two occurs when $f_8^{\leftarrow}$ is small and the exchange approaches unidirectionality. In scheme **II**, the flow through the isotopomer

path $\lambda_{Q1 \rightarrow C1} = 0$. However, a positive net flux will ensure flow through the isotopomer path, $\lambda_{Q1 \rightarrow C1}$, in scheme **I**.

Combining the basic isotope balances and eliminating unbounded terms produces the following two isotope balances around **C1**:

$$\textbf{I:} \quad \beta_C \cdot C1 = \left(\frac{f_8^{net} + \alpha_{EO}}{\beta_E^{net} + \alpha_{EO}} \right) \left(\frac{f_5}{\beta_O^{net}} \right) Q1 \cdot f_9 \tag{24}$$

$$\textbf{II:} \quad \beta_C \cdot C1 = \left(\frac{\beta_O^{net} \cdot \alpha_{EO}^*}{\beta_E^{net} + \alpha_{EO}} \right) \left(\frac{f_5}{\beta_O^{net}} \right) Q1 \cdot f_9 \tag{25}$$

The right hand sides of Eqs. (24) and (25) are $\lambda_{Q1 \rightarrow C1}$. When unidirectional, a_{EO} will approach zero, Eq. (24) will approach Eq. (16), and Eq. (25) will approach zero.

2. Approach

The α_{EO} notation was introduced without explanation of the EO subscript. Designating f_8 as an exchange flux in Fig. 10 had a single effect on the algebraic form of Eq. (16); α_{EO} was added to the denominator, producing Eq. (20). In this way, α_{EO} "compensates" β_E for the presence of the exchange flux. Because α_{EO} is dependent on the value of β_O^{net}, α_{EO} is the association factor that compensates the throughput of **E** with the throughput of **O**.

In all previous examples there was a single isotope source. In the pathway model there are many isotope sources, including labeled feeds, observable isotopomers, and quasi-observables. It is conceivable that two isotopomer paths will be traced in opposite directions through an exchange flux. Therefore, two association factors are needed, one to compensate β_E with β_O^{net}, and one to compensate β_O with β_E^{net}. Figure 13 demonstrates two approaches to the same exchange flux.

60

Figure 13.

The two isotope paths into P1, $\lambda_{Q1 \to P1}$ and $\lambda_{C1 \to P1}$, are written together in the isotope balance around P1, with the addition of a new association factor, α_{OE}. (26)

$$\beta_P \cdot P1 = \left(\frac{f_{10}}{\beta_E^{net} + \alpha_{EO}} \right) Q1 \cdot f_9 + \left(\frac{\beta_E^{net} \cdot \alpha_{OE}^*}{\beta_O^{net} + \alpha_{OE}} \right) \left(\frac{f_{10}}{\beta_E^{net}} \right) C1 \cdot f_6 \qquad (27)$$

$$\alpha_{OE} = \frac{f_8^{\leftarrow}}{\beta_E} \left(\beta_E^{net} - f_8^{net} \right) \qquad (28)$$

The two association factors for an exchange flux are not independent. Only one is needed to describe the reversibility of the exchange flux. After rearrangement, the relation between the normalized association factors is

$$\frac{\alpha_{EO}^* \left(1 - \alpha_{OE}^* \right)}{\alpha_{OE}^* \left(1 - \alpha_{EO}^* \right)} = \frac{\beta_E^{net}}{\beta_O^{net}} \qquad (29)$$

The relation between the dimensional association factors can be found from Eq. (29).

To distinguish the two orientations, the association factors for an exchange flux are designated *proximal* and *distal*. The proximal association factor, α_{EO}, compensates the metabolite at the origin of the net direction, **E**, and the distal association factor, α_{OE}, compensates the metabolite at the terminus, **O**.

3. Implementation: Considering All Possible Orientations

An additional rule is necessary to include exchange fluxes into the tracing algorithm: an isotopomer path cannot pass an exchange flux more than once. For each flux back-step, all previous steps of the path must be checked to see if the next step has already been taken. Any flux already crossed by the path is prohibited from being in the next flux back-step. This rule prevents infinite path looping, in a similar manner to the inclusion of quasi-observable isotopomers.

61

The most significant effect of exchange fluxes on the tracing algorithm is implemented when an isotopomer path is recorded. Exchange fluxes affect isotopomer paths in a manner similar to branched metabolites--they dilute the isotope flow. For both, the dilution fraction has the same general form, the ratio of a flux to a throughput, $\left(\frac{flux}{throughput}\right)$.

The possible orientations of an exchange flux in an isotope path are given in Fig. 14.

Figure 14.

Only four rules are necessary to translate the different orientations into an algebraic form that can be incorporated into $\underline{\Theta}$. When an acceptable path is found, each metabolite is checked to determine whether it is adjacent to an exchange flux. The orientation designates which fluxes and throughputs are incorporated into $\underline{\Theta}$. Note that an exchange flux adjacent to a source metabolite, orientation 1, does not affect the isotopomer path.

Rule I: If the metabolite is the second metabolite of an embedded exchange flux, orientation 2, the dilution fraction is identical to a branch: (f_k^{outlet} / β_k).

Rule II: If the metabolite is adjacent to an exchange flux and it is neither a source nor a target, orientation 3, the dilution fraction is $[f_k^{outlet} / (\beta_k + \alpha_{kx})]$. This is the same as Eq. (20).

Rule III: If the metabolite is the first metabolite of an embedded exchange flux, orientation 4, the dilution fraction will depend on the net direction. If the isotope path is in the same direction as the net direction, scheme **I**, the dilution fraction is

$\left[\left(f_k^{net} + \alpha_{proximal}\right) \middle/ \left(\beta_{proximal}^{net} + \alpha_{proximal}\right)\right]$. If it is in the opposite direction, scheme **II**, the

dilution fraction is $\left[\left(\beta_{proximal}^{net} \cdot \alpha_{distal}^*\right) \middle/ \left(\beta_{distal}^{net} + \alpha_{distal}\right)\right]$.

Rule IV: If the target metabolite is adjacent to an exchange flux that is not in the isotope path, orientation 5, the diluted fraction is $[(\beta_k^{net} / (\beta_k^{net} + \alpha_{kx}))]$. This is the only instance that the general form of a flux divided by a throughput is violated.

Orientation 6 violates the previously described superposition rule, because the outlet flux from the source is an exchange flux. The isotope flow out of the exchange is doubly compensated by the association factor. To correct for this an additional rule is added to the tracing algorithm. If an observable isotopomer is encountered on a path immediately following an exchange flux, it is treated as if it was not an observable, and the tracing continues.

By using all of these rules, the $\underline{\Theta}$ given in Eq. (14) can now be formulated for the example in Fig. 2. The diagonal elements of $\underline{\Theta}$ are the isotopomer paths out of the observable isotopomers, i.e. the $\Sigma\lambda_{out}$ terms.

VI. <u>Implementation</u>

Three of the four difficulties of isotopomer based flux analysis have now been addressed: the intractable size, splitting fluxes, and exchange fluxes. The remaining one is joining fluxes, which produce the non-linear element-wise multiplication seen in Eq. (11). A technique similar to the inclusion of guesses for the independent fluxes into $\underline{A}$ is used to include a joining reaction, for example, f_5 (citrate synthase), into $\underline{\Theta}$. In this case, the isotope pattern of $\underline{C}$ is the unknown vector. An initial guess for $\underline{C}$ is made and the

iterative Newton-Raphson multivariate root determination method is used to approach its value. The entire isotopomer vector, $\underline{\omega}$, can be found from $\underline{\Theta}^{-1}$ once $\underline{C}$ is known.

The first step of determining $\underline{C}$ is the determination of the numerical value of $\underline{\Theta}$ from $\underline{f}^{calc}$. The identity matrix, $\underline{I}$, in the lower right corner of $\underline{\Theta}$, in Eq. (14), corresponds to $\underline{C}$. If the inversion of $\underline{\Theta}$ is found by partitioning (Press et al., 1992), only the upper left portion of $\underline{\Theta}$, $\underline{R}$, needs to be inverted.

$$\Theta = \begin{bmatrix} \mathbf{R} & \mathbf{S} \\ \varnothing & \mathbf{I} \end{bmatrix} \qquad \Theta^{-1} = \begin{vmatrix} \mathbf{R}^{-1} & -\mathbf{R}^{-1} \cdot \mathbf{S} \\ \varnothing & \mathbf{I} \end{vmatrix} \tag{30}$$

To proceed, both $\underline{\Theta}^{-1}$ and $\underline{\eta}$ are parsed into subsets:

$$\underline{\underline{\Theta}}^{-1} = \qquad\qquad \underline{\eta} = \{\, \underline{\eta}^*, \mathbf{g} \,\} \tag{31}$$

The guess for the $\underline{C}$ is $\mathbf{g}$. The vector $\underline{\eta}^*$ is the constant upper portion of the supplied isotopomer vector, $\underline{\eta}$. Because only $\underline{C}$ is non-linearly dependent on other isotopomer fractions, the remainder of $\underline{\omega}$ is linearly interrelated. The values of $\underline{A}$ and $\underline{O}$ are calculated using $\mathbf{g}$ and the sub-matrices of $\underline{\Theta}^{-1}$:

$$\underline{A} = \underline{FAL} \cdot \underline{\eta}^* + \underline{FAR} \cdot \mathbf{g} \tag{32}$$

$$\underline{O} = \underline{FOL} \cdot \underline{\eta}^* + \underline{FOR} \cdot \mathbf{g} \tag{33}$$

The error in the guess for $\mathbf{g}$, $\underline{Q}[\mathbf{g}]$, is found by combining Eqs. (11), (32), and (33):

$$\underline{Q}[\mathbf{g}] = \mathbf{g} - \underline{IMM}_{A,C} \cdot (\underline{FAL} \cdot \underline{\eta}^* + \underline{FAR} \cdot \mathbf{g}) * \underline{IMM}_{O,C} \cdot (\underline{FOL} \cdot \underline{\eta}^* + \underline{FOR} \cdot \mathbf{g}) \tag{34}$$

All of the vectors and matrices in Eq. (34) are constant except $\underline{Q}[\mathbf{g}]$ and $\mathbf{g}$. In each Newton-Raphson iteration a new value for $\mathbf{g}$ is found such that $\underline{Q}$ approaches $\underline{0}$ (Press et

al., 1992). The direction for each step of g is determined from a first order approximation to Eq. (34):

$$g^{new} = g^{old} + \underline{J}^{-1} \cdot (-\underline{Q}[g])$$ (35)

where $\underline{J}$ is the Jacobian of $\underline{Q}[g]$ with respect to g. The elements of $\underline{J}$ are given in appendix B. An initial guess, g^0 with equal elements that sum to one was found to be robust. In the example experiment in Fig. 2, all elements of g^0 are 0.125.

For the $\underline{\Theta}$ that corresponds to the first iteration of the simulation in the example experiment, $\underline{Q}[g]$ converged to $\underline{0}$ in two iterations. The resultant $\underline{C}$, is {0.163, 0.291, 0.088, 0.158, 0.039, 0.069, 0.069, 0.123}. Full size models, e.g. Fig. 1, have 64 elements in the $\underline{C}$ and typically converge in three or four iterations. Convergence is approached quickly because each element of $\underline{Q}[g]$ is quadratically dependent on only one element of g. The subsequent $\underline{\omega}$ and $\underline{d}^{calc}$ for the example are {1, 1, 1, 0.62, 0.17, 0.08, 0.13, 0.36, 0.64, 0.45, 0.25, 0.11, 0.19, 0.16, 0.29, 0.09, 0.16, 0.04, 0.07, 0.07, 0.12} and {1, 0.3, 0.4, 0.36, 0.64, 0.62, 0.17, 0.08, 0.13}, respectivley. This produces a least squares error (LSE) of $6.2 \cdot 10^2$. We have thus shown how $\underline{d}^{calc}$ is determined from q_0. One complete iteration of the simulation has now been performed.

To determine the resultant set of fluxes in Fig. 15, 100,000 iterations were performed, which required less than 1 minute on a desktop PC. The final LSE was 1.8 $\cdot 10^{-1}$.

Figure 15.

Monte Carlo simulations determined the errors in the figure. This additional layer of iterations produced the full ellipsoid of sensitivities to each measured value. However, a

single standard deviation is reported for illustrative purposes. These errors can be interpreted as the total error introduced into the flux results due to measurement error, $\underline{\sigma}$.

Individually, the values in Fig. 15 may have little direct significance *per se*. To derive regulation information from flux analysis it is necessary to observe a change in the flux pattern in response to an environmental stimulus. While this is beyond the scope of the current work, we can still draw conclusions about the physiology of our hypothetical culture from the numerical results. The flux to **R**, f_3, is approximately 40% of the consumption of **G**, and the export of **C** from the TCA cycle, f_7, is approximately 25% of the TCA cycle flux, f_5. These relatively large ratios indicate a physical necessity for producing **R** and transporting **C** under the culture conditions. The normalized association factor for the exchange flux, f_8, is approximately 0.6, indicating that the exchange is indeed reversible and relatively rapid. On Fig. 11 the denominator of the dilution fraction is more than halfway from the lower to the upper limit. Under these conditions the enzymes regulating f_8 are futilely consuming energy by shuttling carbon between **E** and **O**. Thus the computation and comparison of fluxes helps to define and understand the physiology of a cell.

Acknowledgements

Appendix A. Determining the Isotopomer of a Source Metabolite Using AMMs

A. Isotopomer notation

There are 2^n isotopomers for a metabolite with n carbons. The presence of ^{13}C and ^{12}C in a metabolite can be represented by a binary number, where a "1" corresponds to ^{13}C and a "0" to ^{12}C, e.g., metabolite **C** with pattern •-o-• is C_{101}. The number of the isotopomer fraction is the corresponding decimal number, i.e., C_5.

Orientation can be confusing with isotopomer notations. In this paper we maintained the following conventions. On vertically drawn metabolites, the top carbon is the first carbon. When observing a horizontally drawn metabolite, the impulse is to label the left-most carbon as the first. However, in a binary number, the first carbon must be the right-most carbon. To prevent the need to "invert" from graphic to numeric notations, in all cartoons of metabolites the right-most carbon is the first carbon. For example, **C** with pattern •-o-o is C_{100}, which is equivalent to C_4.

In this paper isotopomer fractions are written with subscripts, e.g. C_{18}, and fractional enrichments are not, e.g. C2.

B. Determining the Isotopomer of a Source Metabolite

The isotopomer number is first converted into binary notation, e.g. C_5 into C_{101}. A vector is constructed of the digits of the binary number, $\widehat{C} = \{1, 0, 1\}$. This vector is multiplied by the transpose of the AMM corresponding to the flux.

$$\underline{\underline{AMM}}_{X \to C} = \begin{bmatrix} 0 & 0 & 1 \\ 1 & 0 & 0 \\ 0 & 1 & 0 \end{bmatrix} \qquad \underline{\widehat{X}} = \underline{\underline{AMM}}^T_{X \to C} \cdot \underline{\widehat{C}} \qquad \begin{Bmatrix} 1 \\ 1 \\ 0 \end{Bmatrix} = \begin{bmatrix} 0 & 1 & 0 \\ 0 & 0 & 1 \\ 1 & 0 & 0 \end{bmatrix} \cdot \begin{Bmatrix} 1 \\ 0 \\ 1 \end{Bmatrix} \qquad (36)$$

The transpose is used because paths are traced from product to substrate, and AMMs are defined in the opposite direction. The isotopomer of the source is now found by converting the vector to decimal form, X_6.

Appendix B. Details of the Newton-Raphson method for determining the Citrate isotopomer fraction vector

The constant terms in Eq. (34) are lumped together to simplify the notation:

$$\underline{IFAL\eta} = \underline{IMM}_{A \rightarrow C} \cdot \underline{FAL} \cdot \underline{\eta}^* \qquad \underline{IFAR} = \underline{IMM}_{A \rightarrow C} \cdot \underline{FAR}$$

$$\underline{IFOL\eta} = \underline{IMM}_{O \rightarrow C} \cdot \underline{FOL} \cdot \underline{\eta}^* \qquad \underline{IFOR} = \underline{IMM}_{O \rightarrow C} \cdot \underline{FOR} \qquad (37)$$

The isotopomer-mapping matrices $\underline{IMM}_{A \rightarrow C}$ and $\underline{IMM}_{O \rightarrow C}$ in Eq. (37) are

$$\underline{IMM}^T_{A \rightarrow C} = \begin{bmatrix} 1 & 0 & 1 & 0 & 1 & 0 & 1 & 0 \\ 0 & 1 & 0 & 1 & 0 & 1 & 0 & 1 \end{bmatrix} \qquad \underline{IMM}^T_{O \rightarrow C} = \begin{bmatrix} 1 & 1 & 0 & 0 & 0 & 0 & 0 & 0 \\ 0 & 0 & 1 & 1 & 0 & 0 & 0 & 0 \\ 0 & 0 & 0 & 0 & 1 & 1 & 0 & 0 \\ 0 & 0 & 0 & 0 & 0 & 0 & 1 & 1 \end{bmatrix} \qquad (38)$$

The elements of $\underline{J}$ are then

$$J_{i,j} = \frac{\partial Q_i}{\partial g_j} = \begin{vmatrix} -\left[\Delta + IFAR_{i,j} \cdot \left(\underline{IFOR} \cdot \underline{g} \right)_i + IFOR_{i,j} \cdot \left(\underline{IFAR} \cdot \underline{g} \right)_i \right] & i \neq j \\ 1 - \left[\Delta + IFAR_{i,j} \cdot \left(\underline{IFOR} \cdot \underline{g} \right)_i + IFOR_{i,j} \cdot \left(\underline{IFAR} \cdot \underline{g} \right)_i \right] & i = j \end{vmatrix}$$

$$\Delta = const = \left(IFOR\eta_i \cdot IFAR_{i,j} + IFAL\eta_i \cdot IFOR_{i,j} \right) \qquad (39)$$

Equations (35) and (39) are implemented by an iterative computational method. First, an initial guess, $\underline{g}$, is made. From $\underline{\Theta}$, the constant matrices, $\underline{IFAL\eta}$, $\underline{IFOL\eta}$, $\underline{IFAR}$, and $\underline{IFAR}$ are found using Eq. (37). Equation (39) is used to find $\underline{J}$ from $\underline{g}$, which is inverted to determine $\underline{g}^{new}$ using Eq. (35). $\underline{g}^{new}$ becomes $\underline{g}^{old}$ for the next iteration. Iterations are repeated until $\underline{Q}[\underline{g}] = \underline{0}$.

Nomenclature

α	association factor
α^*	normalized association factor
A, **C**, **E**, **O**	isotopomer fraction vectors
A	stoichiometric matrix
AMM	Atom mapping matrix
β_X	metabolite throughput of X
β_X^{net}	bounded, net-based metabolite throughput of X
b	constraint vector
$\underline{\mathbf{d}}^{meas}$	vector of measured variables
f_i	metabolic flux i
f_i^{net}	bounded net-based metabolic flux i
$f_i^{\rightarrow}$	forward flux of an exchange reaction
$f_i^{\leftarrow}$	backward flux of an exchange reaction
f	flux vector
g	guess for citrate (**C**) isotopomer fraction vector
$\underline{\Theta}$	isotopomer matrix
IMM	isotopomer mapping matrix
K	number of branch metabolites in an isotope path
λ_i	flux through an isotopomer path
$\underline{\eta}$	isotopomer input vector
Oi	fractional enrichment of the ith carbon of **O**
$\mathbf{q}_0$	guess for independent fluxes
$\underline{\mathbf{Q}}[\mathbf{g}]$	error in the guess for **g**
$\underline{\sigma}$	vector of standard deviations of the measured variables
ν	stoichiometric ratio
$\underline{\omega}$	isotopomer vector

69

References

Forbes NS, Clark DS, Blanch HW. 2000. Analysis of metabolic fluxes in mammalian cells. In: Schügerl K, Bellgardt KH, editors. Bioreaction engineering. Modeling and control. Berlin: Springer. Chap 4.4. Appearing Aug. 28, 2000.

Goel A, Ferrance J, Jeong J, Ataai MM. 1993. Analysis of metabolic fluxes in batch and continuous cultures of *Bacillus subtilis*. Biotechnol. Bioeng. **42**: 686-696

Jorgensen H. 1995. Metabolic flux distributions in *Penicillium chrysogenum* during fed-batch cultivations. Biotechnol. Bioeng. **46**: 117-131.

Klapa MI, Park SM, Sinskey AJ, Stephanopoulos G. Metabolite and isotopomer balancing in the analysis of metabolic cycles: I. Theory. Biotechnol. Bioeng. **62**: 375-391.

Portais JC, Schuster R, Merle M, Canioni P. 1993. Metabolic flux determination in C6 glioma cells using carbon-13 distribution upon [1-^{13}C] glucose incubation. Eur. J. Biochem. **217**: 457-468.

Press WH, Teukolsky SA, Vetterling WT, Flannery BP. 1992. Numerical Recipes in C. Cambridge: Cambridge University Press. 994 p.

Schmidt K, Carlsen M, Nielsen JØ, Villadsen J. 1997. Modeling isotopomer distributions in biochemical networks using isotopomer mapping matrices. Biotechnol. Bioeng. **55**: 831-840.

Schmidt K, Nørregaard LC, Pedersen B, Meissner A, Duus JO, Nielsen JØ, Villadsen J. 1999. Quantification of intracellular metabolic fluxes from fractional enrichment and ^{13}C-^{13}C coupling constants on the isotopomer distribution in labeled biomass components. **1**: 166-179.

Schmidt K, Nielsen JØ, Villadsen, J. 1999. Quantitative analysis of metabolic fluxes in Escherichia coli, using two-dimensional NMR spectroscopy and complete isotopomer models. J. Biotech. **71**: 175-189.

Sharfstein ST, Tucker SN, Mancuso A, Blanch HW, Clark DS. 1994. Quantitative in vivo nuclear magnetic resonance studies of hybridoma metabolism. Biotechnol. Bioeng. **43**: 1059-1074.

Vallino JJ, Stephanopoulos G. 1992. Metabolic flux distribution in *Corynebacterium glutamicum* during growth and lysine overproduction. Biotechnol. Bioeng. **41**: 633-646.

Wiechert W, de Graaf AA. 1997. Bidirectional reaction steps in metabolic networks: I. Modeling and simulation of carbon isotope labeling experiments. Biotechnol. Bioeng. **55**: 101-117.

Wiechert W, Möllney M, Isermann N, Wurzel M, de Graaf AA. 1999. Bidirectional reaction steps in metabolic networks: III. explicit solution and analysis of isotopomer labeling systems. Biotechnol. Bioeng. **66**: 69-85.

Zupke C, Stephanopoulos G. 1994. Modeling of isotope distribution and intracellular fluxes in metabolic networks using atom mapping matrices. Biotechnol. Prog. **10**: 489-498.
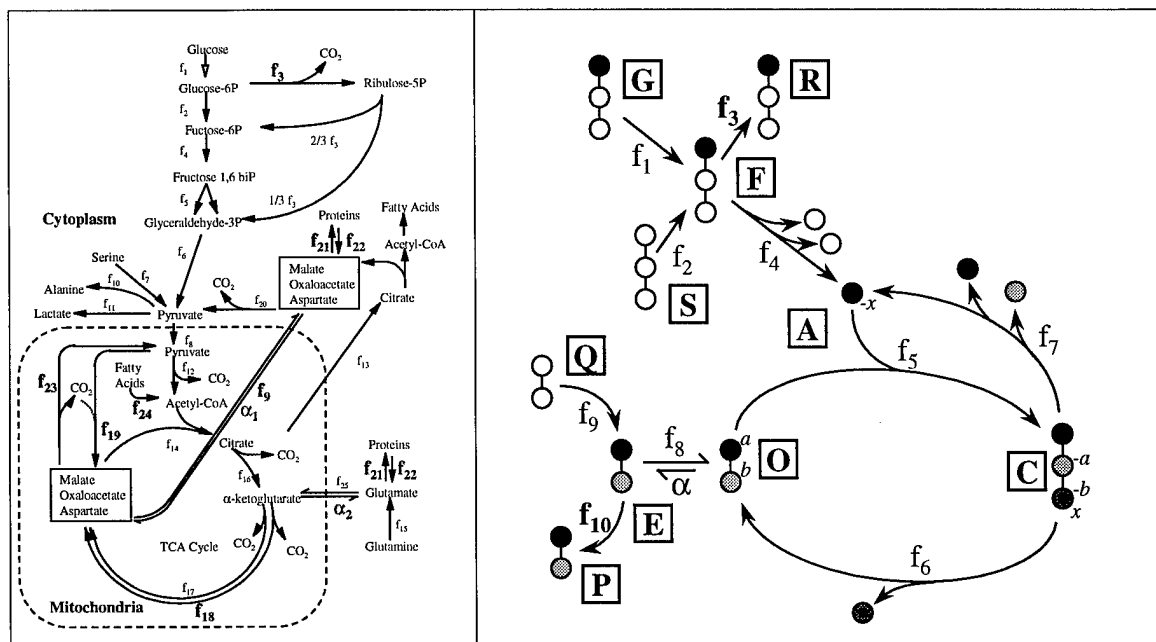
List of Figures

Figure 1. Example Pathway Model
Contains mitochondrial compartmentalization. Independent fluxes are in bold case.

Figure 2. Abbreviated Pathway Model
Each circle represents a carbon atom. The shaded circles are partially enriched by ^{13}C. Differential shading indicates carbon of origin. In f_5 and f_7, -a, -b, and -x originated from a, b, and x, respectively. All metabolites in this model contain half the number of carbons for mathematical brevity. The carbon atoms of each metabolite are numbered from the top. An example of each pathway complexity is included: a splitting flux (f_4), a joining flux (f_5), a cyclic pathway (f_5 & f_6), and an exchange flux (f_8). The half-length metabolites are analogs of: G-glucose, S-serine, R-ribose, A-acetyl-CoA, C-citrate, O-oxaloacetate/malate, E-glutamate/aspartate, Q-glutamine, and P-cellular protein

Figure 3. Example of a Branched Pathway
This figure is a simplification of the glycolytic region of Fig. 2. Each circle represents a carbon atom; the darkened circles are partially enriched by ^{13}C. As before, the three carbon atoms of each molecule are numbered 1 - 3 starting at the top.

Figure 4. Flow Chart of the Solution Method
All inputs to the system are highlighted boxes. The two main boxes represent the two segments of the method. The left box is the tracing algorithm. The right box is the simulation algorithm. The simulation is a nested hierarchy of linear and non-linear components. $\underline{A}$, $\underline{O}$ and $\underline{d}^{calc}$ are all subsets of $\underline{\omega}$. The "*" symbol indicates element-wise vector multiplication.
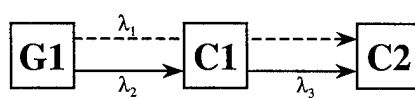
Figure 5. Isotopomer Flux Superposition
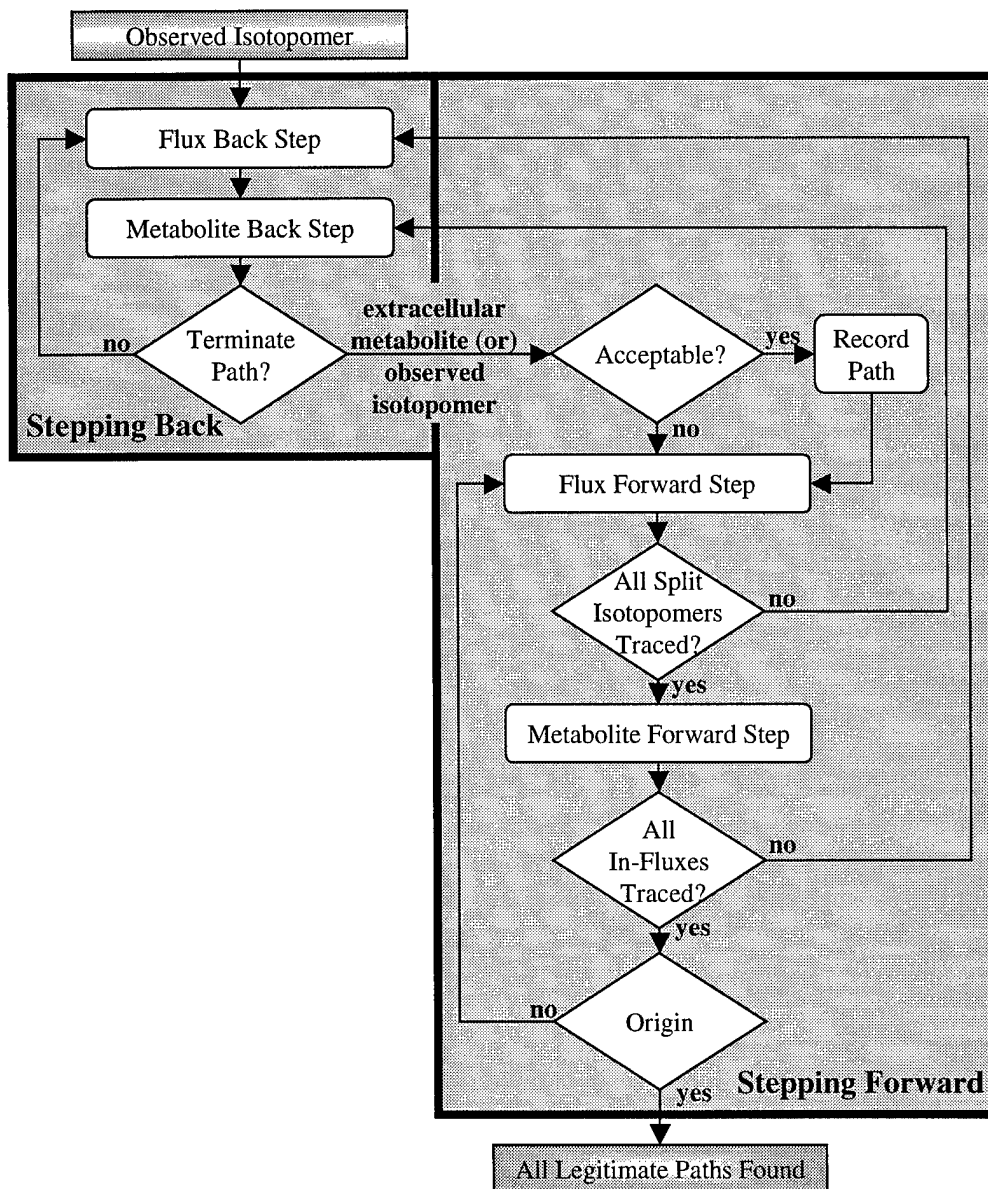
Figure 6. Algorithm for Isotopomer Path Tracing

Figure 7. The Three Steps of One Tracing Iteration
1) An in-flux is chosen, f_4. 2) The flux is traced to its source metabolite, F. 3) The isotopomer of the source is determined, F_1. The source is checked to determine if it is an observed isotopomer or an extracellular metabolite. In this example it is neither. This diagram represents the Stepping Back portion of the tracing algorithm in Fig. 8.

Figure 8. Example of a Splitting Flux
The isotopic composition of the alternate product, i.e., the metabolite not in the isotope path, X, of a splitting flux is undefined.

Figure 9. Combination of Paths into a Joining Flux

Every combination of paths producing the substrates of a joining flux affects the isotopomer distribution of the product

Figure 10. Excerpt of the Exchange Flux from Fig. 2

For illustrative purposes, isotope is incorporated into Q on the first carbon. It is assumed that none of the reactions scramble carbons.

Figure 11. The Denominator of the Dilution Fraction in Equation 30

The denominator is plotted as a function of the throughputs, β_E^{net} and β_O^{net}; the net flux, f_8^{net}; and the extent of the exchange, $f_8^{\leftarrow}$.

Figure 12. An Exchange Flux Embedded in an Isotopomer Path

Figure 13. The Two Approaches to an Exchange Reaction

Each of the possible approaches requires an association factor.

Figure 14. The Six Orientations of Exchange Fluxes in Isotopomer Paths

Each panel represents an isotopomer path. X's are source metabolites; circles with dots ($\odot$) are observed isotopomers; and open circles ($\bigcirc$) are metabolites that are neither sources nor targets. Shading indicates metabolite of interest.

Figure 15. Flux Results for the Example Experiment

Figure 1. Example Pathway Model Contains mitochondrial compartmentalization. Independent fluxes are in bold case.

Figure 2. Abbreviated Pathway Model
Each circle represents a carbon atom. The shaded circles are partially enriched by ^{13}C. Differential shading indicates carbon of origin. In f_5 and f_7, -a, -b, and -x originated from a, b, and x, respectively. All metabolites in this model contain half the number of carbons for mathematical brevity. The carbon atoms of each metabolite are numbered from the top.
An example of each pathway complexity is included: a splitting flux (f_4), a joining flux (f_5), a cyclic pathway (f_5 & f_6), and an exchange flux (f_8). The half-length metabolites are analogs of: G-glucose, S-serine, R-ribose, A-acetyl-CoA, C-citrate, O-oxaloacetate/malate, E-glutamate/aspartate, Q-glutamine, and P-cellular protein.

Figure 3. Example of a Branched Pathway
This figure is a simplification of the glycolytic region of Fig. 2. Each circle represents a carbon atom; the darkened circles are partially enriched by ^{13}C. As before, the three carbon atoms of each molecule are numbered 1 - 3 starting at the top.

Initial Guess $\underline{q}_0$

Simulated Annealing

$\underline{b} = [\, \varnothing \mid \underline{q}\,]$

Pathway Model $\underline{\underline{A}}$

Calculate Guessed Fluxes
$\underline{f}^{calc} = \underline{\underline{A}}^{-1} \cdot \underline{b}$

Function Form of
Isotopomer Matrix $\underline{\Theta}(\underline{f})$

Invert Numerical Isotopomer
Matrix $\underline{\Theta}^{-1}$

Isotopomer Path Tracing

Newton-Raphson Method

AMMs

$\underline{\omega} = \underline{\Theta}^{-1} \cdot [\, \underline{n}^* \mid \underline{C}\,]$

Supplied Isotopomers $\underline{n}^*$

$\underline{A}, \underline{O} \subset \underline{\omega}$

$\underline{C} = \underline{\underline{IMM}}_{A \to C} \cdot \underline{A} * \underline{\underline{IMM}}_{O \to C} \cdot \underline{O}$

Isotopomer Pattern $\underline{\omega}$

non-linear

linear

$\underline{d}^{calc} \subset \underline{\omega}$

Measurements $\underline{d}^{meas}$

$LSE = \sum (\underline{d}^{meas} - \underline{d}^{calc})^2 \big/ \underline{\sigma}^2$

Result $\underline{f}$

"Mutate" Independent Fluxes $\underline{q}$

Repeat N Times $\rightarrow$

non-linear

Figure 4. Flow Chart of the Solution Method
All inputs to the system are highlighted boxes. The two main boxes represent the two segments of the
method. The left box is the tracing algorithm. The right box is the simulation algorithm. The
simulation is a nested hierarchy of linear and non-linear components. $\underline{A}$, $\underline{O}$ and $\underline{d}^{calc}$ are all subsets of
$\underline{\omega}$. The "*" symbol indicates element-wise vector multiplication.

Figure 5. Isotopomer Flux Superposition

Figure 6. Algorithm for Isotopomer Path Tracing

77

Figure 7. The Three Steps of One Tracing Iteration
1) An in-flux is chosen, f_4. 2) The flux is traced to its source metabolite, F. 3) The isotopomer of the source is determined, F_1. The source is checked to determine if it is an observed isotopomer or an extracellular metabolite. In this example it is neither. This diagram represents the Stepping Back portion of the tracing algorithm in Fig. 8.

78

Figure 8. Example of a Splitting Flux
The isotopic composition of the alternate product, i.e., the metabolite not in the isotope path, X, of a splitting flux is undefined.

Figure 9. Combination of Paths into a Joining Flux
Every combination of paths producing the substrates of a joining flux affects the isotopomer
distribution of the product

Figure 10. Excerpt of the Exchange Flux from Fig. 2
For illustrative purposes, isotope is incorporated into Q on the first carbon. It is assumed that none of the reactions scramble carbons.

Figure 11. The Denominator of the Dilution Fraction in Equation 30
The denominator is plotted as a function of the throughputs, $\beta_E{}^{net}$ and $\beta_O{}^{net}$; the net flux, $f_8{}^{net}$; and the extent of the exchange, $f_8{}^{\leftarrow}$.
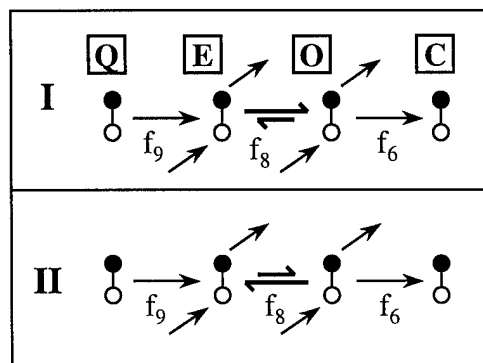
Figure 12. An Exchange Flux Embedded in an Isotopomer Path

Figure 13. The Two Approaches to an Exchange Reaction
Each of the possible approaches requires an association factor.
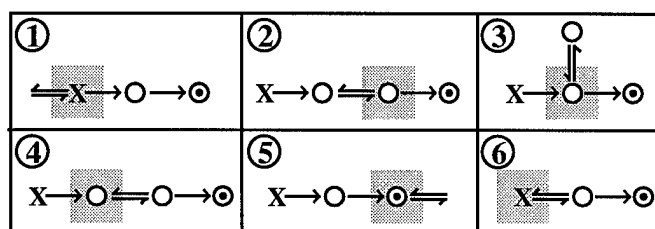
Figure 14. The Six Orientations of Exchange Fluxes in Isotopomer Paths
Each panel represents an isotopomer path. X's are source metabolites; circles with dots (⊙) are observed isotopomers; and open circles (○) are metabolites that are neither sources nor targets. Shading indicates metabolite of interest.
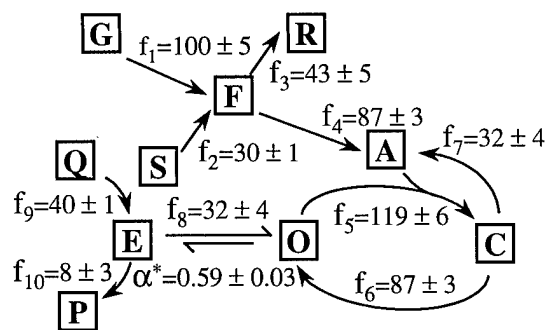
Figure 15. Flux Results for the Example Experiment

Effects of Hypoxia on Tamoxifen Response of MCF7 Human Breast Cancer Cells in Microcarrier Culture

Kimberly A. Wicklund, Harvey W. Blanch, and Douglas S. Clark, Department of Chemical Engineering, University of California-Berkeley, CA 94720

ABSTRACT

The effect of reduced oxygen tension on the action of the hormonal therapeutic tamoxifen was investigated in microcarrier cultures of MCF7 human breast cancer cells. After five days, TAM-treated cultures grew to 30% and 75% of vehicle control cultures in 20% (normoxic) and 2% (hypoxic) oxygen, respectively. The decreased effect on cell growth seen in hypoxic conditions was due to the reduced rate of growth of control cultures; TAM final cell density was not affected by oxygen level. Cells were distributed similarly among cell cycle phases, exhibiting a holdup in G0-G1, in control cultures in 2% oxygen and in TAM-treated cultures irrespective of oxygen level. In 20% oxygen, TAM decreased glucose metabolism as reported previously in the literature. Specifically, glucose uptake and lactate dehydrogenase (LDH) activity were reduced to In 2% oxygen, this effect was retained only when waste products were removed and media replenished. Hypoxia did increase glucose uptake, lactate production, lactate dehydrogenase (LDH) activity, and pyruvate kinase (PK) activity compared to that seen in normoxia, even in the presence of TAM. Thus, the decreased glucose metabolism caused by TAM in normoxic conditions can be overcome when subjected to hypoxic conditions. This is the first *in vitro* study aimed to understand the action of TAM on growth and metabolism at physiologically relevant levels of oxygen. This model may be used to examine unexplained actions of TAM seen in patients, such as the "metabolic flare" reaction observed by Deshdati *et al.*

INTRODUCTION

Much cancer research concerning therapeutics testing and development is conducted in monolayer tissue cultures. The environment of these tissue cultures is radically different than that of an actual tumor. The irregular vascular networks of tumors give rise to regions of inadequate nutrient and oxygen supply and waste removal (1-3). Often, tumors develop hypoxic regions where oxygen concentrations may be less than 0.1% (3-5). Also, glucose levels may approach zero and extracellular pH may be low (6-10). This is due to the up-regulation of glycolysis under hypoxic conditions and the resulting accumulation of lactate (3, 11). Conversely, tissue cultures are generally maintained in nutrient-rich media in an oxygenated environment. The role of the tumor microenvironment has been found to be significant in the failure of some treatment strategies(12-15). For example, hypoxic conditions induce cell cycle arrest, conferring resistance to conventional chemotherapeutics that act on rapidly dividing cells (16).

Tamoxifen (TAM) is the most widely used hormonal therapeutic for advanced breast cancer. TAM is most effective against estrogen receptor-positive tumors (ER+), with 30 and 50% of pre- and post-menopausal patients responding, respectively. It is significantly less effective against estrogen receptor-negative (ER-) tumors, yielding response rates of approximately 10% (17). Although other mechanisms of action are reported to exist (18-20), TAM appears to act primarily as a competitive inhibitor of estrogen binding to the estrogen receptor, thus preventing the proliferative effects of estrogen (21, 22). As a result, TAM has a cytostatic effect on growth, and cells accumulate in the G0/G1 phase of the cell cycle (23, 24).

In order to accommodate increased proliferation, estrogen exerts effects on metabolism. For example, in human breast cancer cells grown in culture or as tumors implanted in nude mice, estrogen treatment results in an increased flux through energy-

generating and biosynthetic pathways (25-28). TAM, however, has conflicting effects in cells grown in culture or as tumors implanted in nude mice compared to that seen in human patients. *In vitro*, TAM treatment causes decreased glucose uptake, lactate release, and activity of some glycolytic enzymes, such as lactate dehydrogenase (LDH) (25, 26, 29). However, uptake of the glucose analog fluoro-deoxyglucose was measured in patients with advanced metastatic disease, and it was found that the tumors of responding patients actually exhibited an increased uptake rate after ten days of TAM treatment. This subclinical condition was termed "metabolic flare" (30). The cause of this difference in glucose metabolism between cell model systems and human patients under the influence of TAM is not known.

As stated above, TAM is reported to have mechanisms of action that are independent of the estrogen receptor. One such mechanism is the inhibition of angiogenesis, though this is not without controversy (31-36). This inhibition would presumably decrease tumor oxygenation, and indeed this was demonstrated in MCF-7 xenografts and chick egg chorioallantoic membranes (31, 33). However, the impact of hypoxia on TAM efficacy and action is unknown. This work seeks to understand how availability of oxygen affects the growth, metabolite utilization, and enzyme activities of TAM-treated cells *in vitro*, using MCF7 human breast cancer cells in microcarrier culture.

MATERIALS AND METHODS

Cell Culture

Culture of Stock Cells. MCF7 human breast cancer cells were obtained from Dr. Gary Firestone (University of CA-Berkeley, Dept. of Molecular and Cellular Biology) at passage 22. Cells were maintained routinely as monolayer cultures in plastic T-150

flasks (Corning Inc., Corning, NY). Cells were grown in DMEM (1 g/L glucose), pH 7.1, supplemented with 5% FBS (Sigma, St. Louis, MO) in a humidified atmosphere of 5%CO_2 in air at 37°C. Cells were subcultured every five days using trypsin/EDTA (UC-San Francisco Cell Culture Facility).

Microcarrier Culture Experiments. Experiments were performed in 500 mL spinner flasks (Bellco, Vineland, NJ). Flask caps were modified to allow the attachment of 12 mm Clark-type dissolved oxygen probes (Mettler-Toldedo, Wilmington, MA). Sidearm caps were modified to allow sterile headspace gassing. Cultures were initiated in 2/5 of the final culture volume with intermittent stirring at 45 rpm for 1 minute every half hour during the first four hours, after which time cultures were constantly stirred. Approximately 3.0×10^7 cells were inoculated in 0.33 g pre-swelled Cytodex 3 microcarriers (Pharmacia, Uppsala, Sweden) and 200 mL DMEM (1g/L glucose) supplemented with 5% FBS, yielding a seeding density of 17,000 cells/cm^2. Upon initiation of cell cultures, headspaces were continually gassed with 5% CO_2, 95% air. Twenty-four hours after initial seeding, beads were allowed to settle and media was removed and replaced with 500 mL of the medium of interest, denoting day 0. Cell density on day 0 ranged from 50,000-70,000 cells/ml. Medium of interest consisted of DMEM with 1.0 g/L glucose, 5% FBS, and either 1μM tamoxifen (Sigma, St. Louis, MO) or 0.02% (wt./vol.) absolute ethanol vehicle control. After feeding, flask headspaces were gassed with 5% CO_2, balance gas of interest. For hypoxic experiments, the gas composition was 5%, 2% O_2, balance N_2. Normoxic experiments were done under 5% CO_2, balance air. Equilibrium with the gas mixture was obtained approximately 6 hours after feeding. A hypoxic experiment with an additional feeding on day 3 was performed

to investigate the effects of waste removal and nutrient replenishment, since there was significant accumulation of lactate and depletion of glucose in hypoxic experiments. The medium used for this second feeding was pre-equilibrated with 5% CO_2, 2% O_2, balance N_2. In addition, flasks were gassed during media replacement to minimize exposure to oxygen while feeding. Cultures were maintained at 37°C. To monitor cultures, triplicate samples were withdrawn daily under constant stirring. Dissolved oxygen level was noted before and after sampling. The dissolved oxygen levels were not significantly affected by the sampling procedure; sidearm gassing was performed during sampling to minimize exposure to room air. Samples were centrifuged at 80 g for 10 minutes, and supernatents were frozen at -15°C for subsequent analysis. Cell/microcarrier pellets were stored at -80°C to preserve cell nuclei and enzyme activity. Each set of experiments (one flask each vehicle control and 1 μM TAM) was performed in duplicate using different passage numbers to initiate the cultures. Analyses were performed in triplicate for individual cultures.

Analytical Methods

Cell Growth and Morphology. Cell growth was monitored by counting released nuclei on a hemacytometer according to the method of Lin *et.* al (37). Cell cycle phase distribution was measured using flow cytometry (Epics-XL, Coulter Cytometry, Hialeah, FL). Cell nuclei were released and stained with a solution of 75 μM propidium iodide, 0.1% sodium citrate, 0.1% Triton X-100 (Sigma, St. Louis, MO) at a final concentration of approximately 1×10^6 nuclei/ml. Prior to analysis, samples were filtered through 60 μm nylon mesh (Tetko, Inc., Kansas City, MO) to remove microcarriers and other debris. Ten

thousand stained nuclei were analyzed to produce a histogram. Fluorescence histograms were analyzed using MCycle software (Phoenix Flow Systems, Inc., San Diego, CA).

Metabolite Analyses. Glucose, lactate, and glutamine concentrations were determined using a biochemistry analyzer (model 2700 Select, Yellow Springs Instrument Co., Inc.,Yellow Springs, OH). Specific metabolite uptake rates on days 2 and 5 were calculated by fitting four to five data points linearly. The resulting slope was divided by the cell density in order to obtain a specific metabolite uptake or production rate. pH was measured using a pH electrode (model 39847, Beckman Instruments, Fullerton, CA) coupled to a pH/ISE meter (model Φ12, Beckman Intstruments, Fullerton, CA). pH determinations were made immediately upon sample removal.

Enzyme Activity Determinations. Cell/microcarrier pellets were resuspended in 1 volume of homogenization buffer containing 10 mM Tris, 0.1 mM DTT, pH 7.4 (Sigma, St. Louis, MO). Extracts were obtained by performing fifty strokes in a Dounce homogenizer. Protein measurements were performed using the commercially available BCA assay (Pierce, Rockford, IL). G6PDH activity was measured using a commercially available kit based on UV spectrophotometric absorbtion of NADPH. LDH activity was measured using a commercially available kit based on colorometric absorption of pyruvate reacted with 2,4-dinitrophenylhydrazine. This same kit was adapted to measure PK activity. The assay buffer contained 100 mM Tris, 10 mM $MgCl_2$, 80 mM KCl, 5 mM ADP, and 5mM PEP. The reaction was carried out for 15 minutes at 37°C, and the pyruvate produced was detected colorimetrically after reaction with the phenylhydrazine reagent from the LDH kit. All reagents and assay kits for enzyme determinations were obtained from Sigma, St. Louis, MO.

RESULTS

Cell Growth and Cell Cycle Distribution. TAM sensitivity, as evidenced by reduction in cell growth compared to vehicle control, decreased under hypoxic conditions. TAM alone, hypoxia alone, and their combination reduced cell growth compared to normoxic vehicle control cultures. The effect was apparent after two days in culture, and significant reduction was seen after five days in culture. TAM addition to the medium significantly reduced the final cell density in normoxic conditions, but had lessened effect in hypoxic conditions with and without media replenishment (Fig.1). The decreased sensitivity to TAM of hypoxic cultures is a result of decreased growth of hypoxic control cultures compared to normoxic control cultures; the growth of TAM-treated cultures was unaffected by oxygen level. The final cell density of TAM-treated cultures was only 30% of vehicle control cultures in normoxic conditions, while this value was 55% and 75% of the corresponding vehicle controls in hypoxia with and without media replenishment, respectively.

The decreased growth of hypoxic cells treated with and without TAM and TAM-treated normoxic cells was associated with an increased proportion of cells in G0/G1 and decreased proportion in S phase by day 5 (Fig.2). In all conditions, throughout the course of culture, cell viability was at least 95%, which was evidenced by trypan blue staining. Thus, the increased fraction of cells in G0/G1 was due to hold up in G0/G1, rather than the death of cells in S or G2/M phase. Normoxic control cultures did not exhibit an accumulation of cells in G0/G1, instead the proportion of G0/G1 and S phase cells remained constant from day 2 to day 5.

Glucose Utilization. Representative glucose concentration profiles for normoxic cultures and hypoxic cultures with and without media replenishment are shown in figure

3. Hypoxic cultures consumed considerably more glucose than normoxic cultures, both in the bulk media and on a per cell basis (figure 4). However, glucose concentrations did not fall significantly below 1 mM under any condition and, therefore, were adequate to sustain cell growth. Hypoxia increased glucose metabolism as early as day 2 of culture. This effect was sustained throughout the course of culture; by day 5, the specific glucose uptake of hypoxic vehicle control cultures (0.92 ± 0.08 fmol/cell/day) was almost 2.5 fold higher than normoxic vehicle control cultures (0.41 ± 0.08 fmol/cell/day). In hypoxic vehicle control cultures with media replacement this effect was even more drastic, with a glucose specific uptake rate almost five times that of normoxic vehicle control cultures. Thus, the depletion of glucose and/or buildup of waste products in hypoxic cultures without media replacement adversely impacted the cell's ability to consume glucose.

In normoxic conditions, TAM significantly decreased the specific glucose uptake rate by day 2 (figure 4). TAM had less effect on glucose metabolism in hypoxic conditions as compared to normoxic conditions on day 2. In normoxic conditions, the specific glucose uptake rate in untreated cultures was approximately four-fold higher than that in TAM-treated cultures. The effect in hypoxic conditions was less drastic, where the vehicle control specific glucose uptake rate (4.26 ± 0.42 fmol/cell/day) was less than 1.5-fold higher than that in TAM-treated cultures (3.19 ± 0.21 fmol/cell/day). By the fifth day of culture, TAM effect on specific glucose uptake rate in normoxic conditions subsided somewhat. The glucose specific uptake rate in vehicle control cultures (0.41 ± 0.08 fmol/cell/day) was approximately 2.5-fold that in TAM-treated cultures (0.16 ± 0.08 fmol/cell/day). The degree of downregulation of glucose uptake in hypoxic cultures without media replacement was similar on days 2 and 5. Thus, the effect of TAM on

glucose uptake was greater in normoxic cultures compared to hypoxic cultures without media replacement throughout the course of culture. However, TAM did have a significant effect on glucose uptake in hypoxic cultures with media replacement as measured on day 5. The addition of glucose and removal of waste increased glucose utilization by vehicle control cells to 1.92 ± 0.10 fmol/cell/day, while TAM-treated cells were not significantly affected. Under hypoxic conditions, it appears that TAM has some effects on glucose utilization that are independent of its effects on growth, as glucose metabolism was affected more significantly than cell growth in hypoxic conditions with waste removal.

Lactate Utilization. The increased glucose utilization observed in hypoxic cultures with and without TAM, fed and unfed, was accompanied by increased lactate production (figures 5 and 6). The yield of lactate from glucose was nearly two, approaching the theoretical maximum (assuming no other loss or addition of glycolytic intermediates). Thus, dissolved oxygen levels of 2% inhibit the use of the TCA cycle. In addition, significant lactate accumulation and reduced pH were observed in hypoxic cultures with and without media replenishment. Initial lactate concentration was 1 mM and pH was 7.3 in all cultures. By the fifth day in culture, lactate levels rose to 10.7 mM and 6.5 mM (figure 5A), and pH fell to 7.0 and 6.9 in hypoxic cultures with vehicle control and 1 μM TAM, respectively. In contrast, normoxic cultures had relatively little lactate and hydrogen ion accumulation. In fact, lactate levels in normoxic cultures were kept fairly steady throughout the course of the culture since lactate was consumed after two to three days in culture for both untreated and TAM-treated cells.

Media replenishment alleviated the buildup of lactate in hypoxic cultures. Final lactate levels in hypoxic cultures with media replacement were 7.8 mM in vehicle control

and 3.2 mM in TAM-treated cultures (figure 5B). These levels were 73% and 49% of the levels attained in unfed hypoxic vehicle control and TAM-treated cultures, respectively. The pH of fed cultures was not significantly different from that of unfed cultures, dropping to 7.0 by the fifth day of culture in both vehicle control and TAM-treated flasks.

The effect of TAM on specific lactate production rates closely followed the effect on specific glucose uptake rates in hypoxic cultures with and without media replenishment (figure 6). However, in normoxic cultures, TAM had very little effect on lactate utilization as measured on the fifth day of culture. After two days of TAM treatment, normoxic cells did exhibit reduced lactate production compared to the vehicle control. The degree of reduction was similar to that seen for specific glucose uptake rates.

Glutamine Utilization. Representative glutamine concentration profiles are shown in figure 7. As expected, glutamine utilization was significantly affected by lowered oxygen tension. Hypoxic cells in all conditions utilized glutamine at about half the rate of normoxic cells, with two exceptions (figure 8). On day 2, hypoxic TAM-treated cultures with media replenishment had specific glutamine utilization rates that were statistically insignificant from all other conditions. The value on day 2 should be the same for hypoxic cultures with and without media replenishment, since there are no experimental differences until day 3. However, the large error in specific glutamine uptake rate for fed hypoxic TAM-treated cultures on day 2 renders that value statistically insignificant from all other conditions. Interestingly, on day 5, fed TAM-treated hypoxic cells exhibited a significantly higher rate of glutamine uptake than the corresponding controls and was not significantly different than values seen in both normoxic conditions (control and TAM-treated).

Enzyme Activity. LDH and PK activity measurements are shown in figure 9. Elevated levels of both enzymes were present in hypoxic conditions compared to normoxic conditions, in the presence and absence of TAM. In normoxic conditions, TAM-treated cultures had a significantly lower level of LDH activity on both days 2 and 5, while PK was not affected. In hypoxic conditions without media replacement, TAM had no effect on LDH activity, but caused a 67% reduction in PK activity. In fed cultures, TAM had no effect on either LDH or PK activity on both days 2 and 5.

Summary of Results. The effects of TAM on growth, metabolite utilization, and enzyme activity under normoxic and hypoxic conditions are summarized in Table 1. Since there was no difference between fed and unfed hypoxic cultures on day 2, the data were averaged. TAM effects are shown as the value under TAM treatment expressed as a percent of the value of vehicle control.

DISCUSSION

Estrogen and TAM action has been widely studied using *in vitro* systems, and the MCF-7 human breast cancer cell line is one of the most prevalent model systems (23, 24, 38-40). However, the effect of physiologically relevant levels of oxygen on TAM action *in vitro* has not been previously investigated. Indeed, several studies have investigated TAM action on spheroid cultures, which do have regions of limited oxygen and nutrient supply (41, 42); however, spheroids are heterogeneous with respect to microenvironment, and thus effects of hypoxia can not be determined directly. Growth of cells on microcarrier beads in spinner flasks allowed us to maintain cells in a homogenous environment with respect to oxygenation. In this work, we developed an *in vitro* model system using pertinent levels of oxygen tension that allowed us to further understand TAM effects and identify metabolic parameters that warrant further study concerning

their potential clinical use as determinants of TAM efficacy and as targets for concomitant therapy.

In our hands, MCF7 cells under standard cell culture oxygen tension (20% oxygen in the gas phase) exhibited similar behavior to other reports in the literature for *in vitro* systems. In several reports of cell proliferation experiments using MCF7 monolayer and cultures and human tumor specimens cultured in soft agar, TAM inhibited cell density to a similar degree as seen in our experiments under standard conditions (39, 43, 44). Furman et. al. reported that TAM caused a decrease in growth and a 2-fold decrease in glucose metabolism with only 50% of glucose being utilized via glycolysis in MCF7 cells cultured on microcarriers for approximately 2 days, which is in agreement with our findings (25). Additionally, the effect of TAM under standard oxygen tension on LDH activity was consistent with data reported in the literature (29). The only anomaly detected under normoxic conditions with and without TAM was the uptake of lactate at relatively low lactate levels (<2.5 mM) and in the presence of ample glucose. Lactate utilization was decreased under TAM treatment, a previously unreported action of TAM. In fact, lactate utilization has not been previously reported for the MCF7 cell line regardless of culture system or conditions; however, there have been several reports of lactate uptake in EmT6 spheroids and Jensen sarcoma, Morris hepatoma, Walker sarcocarcinoma, and human breast tumor tissue cultured as implanted tumors in nude rats (7, 45-47). Generally, lactate utilization occurs at elevated levels of lactate; reported "threshold" values (values above which cells switch from lactate production to utilization) range from 2 mM to 15 mM lactate. Presumably, the degree of oxygenation and/or cell type would affect this threshold value, since low oxygen levels would prevent the pyruvate resulting from lactate uptake from entering the Krebs cycle. Thus at higher

oxygen levels, one would expect that lactate utilization would be more prevalent since the pool of pyruvate would be reduced by its entrance into the Krebs cycle. Our results are consistent with this reasoning; however, the reverse trend was shown in EMT6 spheroids, where higher oxygen tensions led to reduced lactate utilization (45). In both our study and that of Bourrat et. al., the fate of the utilized lactate is not known, and thus it is possible that the lactate may be converted into alanine or other amino acids via pyruvate, rather than entering the Krebs cycle, in EMT6 spheroids under lower oxygen tension.

Under oxygen tensions representative of physiological tumor values (2% oxygen in the gas phase), cell density of untreated MCF7s was drastically reduced, approaching that seen in cells arrested with TAM. Cell growth in TAM-treated cultures was insensitive to oxygen level or media replacement, and thus the effect of TAM on cell growth was greatly lessened at reduced oxygen levels. This is yet another indication that care must be taken when using cultures maintained in supraphysiological oxygen tensions to make inferences concerning drug efficacy in humans. Indeed, regression caused by TAM treatment may be less apparent in tumors that have higher levels of hypoxia, since hypoxic cells may already exist in an arrested state. This is also evident in studies performed in implanted MCF7 tumors, where a regression of 40% in tumor size occurred over a period of 30 days. This regression takes place significantly slower than the reduction of cell growth under standard conditions reported here and by others (39, 43, 44).

It is well established that tumor cells have an increased glycolytic capacity in the presence of oxygen when compared to normal cells (48). In reduced oxygen, the glycolytic capacity is increased further, as glucose is the main energy source of tumor cells in hypoxic conditions. Increased activity and expression of certain isoenzymes of

glycolysis, such as pyruvate kinase and lactate dehydrogenase (LDH), allows for increased flux through this pathway, providing energy and biosynthetic precursors. In this study, after 48 hours in culture, MCF7 cells were shown to convert glucose almost exclusively to lactate at 2% oxygen, compared to a 50% utilization of the pathway under standard oxygen tension. The increased utilization of glycolysis under hypoxic conditions was accompanied by an increase of similar magnitude in LDH and PK activities. TAM appeared to retain its effect on glucose uptake when comparing standard and reduced oxygen tensions, as long as waste products were removed and media was replenished. However, in hypoxic conditions, the reduced glucose uptake of TAM-treated cells with media replenishment was not accompanied by a decrease in either PK or LDH activity, and further studies should be undertaken to uncover the mechanism by which TAM reduces glucose uptake in hypoxic conditions. It is interesting to note, however, that under hypoxic conditions glucose uptake was increased in the presence or absence of TAM, and thus TAM's ability to impair glycolysis is somewhat overcome by hypoxia. This is in contrast to TAM's effect on glutamine utilization, where TAM did not significantly affect glutamine uptake under standard oxygen tension, but it enhanced glutamine uptake under hypoxic conditions in fed cultures. The ability of TAM to enhance glutamine uptake has not been reported previously, and should be investigated further, since this observation may point to the use of anti-glutamine therapy as a potential adjuvant therapy.

The motivation to study effects of hypoxia on TAM action partially stems from conflicting reports concerning TAM's effects on angiogenesis and glucose metabolism (25-27, 30-36). To our knowledge, the subclinical "metabolic flare" response observed by Dehdashti, et. al. was contrary to all other reports of TAM action on glucose metabolism.

We hypothesized that this effect may be a result of increased glycolysis caused by decreased oxygen tension. Indeed, an oxygen tension of 2%, which is the value observed in MCF-7 TAM-treated xenografts, caused significantly increased levels of glycolysis. Therefore, the hypothesis that the "metabolic flare" response is a result of increased glycolysis is plausible and warrants investigation *in vivo*. If this response is in fact due to increased glycolysis, "metabolic flare" may be accompanied by decreased pH, increased LDH activity, and increased PK activity, of which, pH could be assessed by noninvasive imaging techniques.

BIBLIOGRAPHY

1. Dewhirst, M., Tso, C, Oliver, R, Gustafson, C Secomb, T and Gross, J Morphologic and hemodynamic comparison of tumor and healing normal tissue microvasculature, Int J Radiat Oncol Biol Phys. *17:* 91-99, 1989.

2. Shah-Yukich, A. a. N., A Characterization of solid tumor vasculature: a three-dimensional analysis using the polymer casting technique, Lab Invest. *58:* 236-244, 1988.

3. Vaupel, P., Kalinowski, F and Okunieff, P Blood flow, oxygen and nutrient supply, and metabolic microenvironment of human tumors: a review, Cancer Research. *49:* 6449-6465, 1989.

4. Nordsmark, M., Bentzen, S, and OVergaard, J Measurement of human tumour oxygenation status by a polarographic needle electrode, Acta Oncol. *33:* 383-389, 1994.

5. Vaupel, P., and Hockel, M Oxygenation status of human tumors: a reappraisal using computerized pO_2 histography. *In:* P. W. Vaupel, Kelleher, D K, and Gunderoth, M (ed.) Tumor Oxygenation, pp. 219-232. Stuttgart: Gustav Fischer Verlag, 1995.

6. Gullino, P. The internal millieu of tumors, Prog Exp Tumors Res. *8:* 1-25, 1966.

7. Kallinowski, F. a. V., P pH distributions in spontaneous and isotransplanted rat tumours, Brit J Cancer. *58:* 314-321, 1988.

8.   Mueller-Klieser, W., Freyer, J, and Sutherland, R Evidence for a major role of glucose in controlling development of necrosis in EMT6/Ro multicell tumor spheroids., Adv Exp Med Bio. *159:* 487-495, 1983.

9.   Martin, G. R. a. J., R.K. Noninvasive measurement of interstitial pH profiles in normal and neoplastic tissue using fluorescence ratio imagin microscopy., Cancer Research. *54:* 5670-5674, 1994.

10.   Tannock, I., and Rotin, D Acid pH in tumors and its potential for therapeutic exploitation, Cancer Research. *49:* 4374-4384, 1989.

11.   Robin, E., Murphy, B, and Theodore, J Coordinate regulation of glycolysis by hypoxia in mammalian cells, J Cell Phys. *118:* 287-290, 1984.

12.   Brown, J. M. a. G., A.J. The unique physiology of solid tumors: opportunities (and problems) for cancer therapy, Cancer Research. *58:* 1408-1416, 1998.

13.   Coleman, C. N. Hypoxia in tumors: a paradigm for the approach to biochemical and physiologic heterogeneity, Journal of the National Cancer Institute. *80:* 310-317, 1988.

14.   Teicher, B. A. Hypoxia and drug resistance., Cancer Metastasis Rev. *13:* 139-168, 1994.

15.   Tomida, A., and Tsuruo, T. Drug resistance mediated by cellular stress response to the microenvironment of solid tumors, Anti-Cancer Drug Design. *14:* 169-177, 1999.

16.   Green, S. L. a. G., A. J. Tumor hypoxia and the cell cycle: implications for malignant progression and response to therapy, The Cancer Journal from Scientific American. *4:* 218-223, 1998.

17. Degregorio, M. W. a. W., V.J. Tamoxifen and breast cancer, p. 112. New Haven and London: Yale University Press, 1994.

18. Su, H. D., Mazzei, G J, Vogler, W R, and Kuo, J F Effect of tamoxifen, a nonsteroidal antiestrogen, on phopholipid/calcium-dependent protein kinase and phosphorylation of its endogenous substrate proteins from the rat brain and ovary, Biochem Pharmacol. *34:* 3649-3653, 1985.

19. O'Brian, C. A., Liskamp, R M , Solomon, D H, weinstein, I B Inhibition of protein kinase C by tamoxifen, Cancer Research. *45:* 2462, 1985.

20. Altan, N., Chen, Yu, Schindler, M, and Simon, S M Tamoxifen ihibits acidification in cells independent of the estrogen receptor, Proc Natl Acad Sci. *96:* 4432-4437, 1999.

21. Dickson, R. B., and Lippman, M E Estrogenic regulation of growth and polypeptide growth factor secretion in human breast carcinoma., Endocrinology Reviews. *8:* 29-43, 1987.

22. Heel, R. C., Brogden, R N, Spreight, T M, and Avery, G S Tamoxifen: a review of its pharmacodynamic and pharmacokinetic properties, and therapeutic use., Drugs. *16:* 1, 1978.

23. Osborne, C. K., Boldt, D H, and Estrada, P Human breast cancer cell cycle synchronization by estrogens and antiestrogens in culture, Cancer Research. *44:* 1433-1439, 1984.

24. Taylor, I. W., Hodson, P J, Green, M D, and Sutherland, R L Effects of tamoxifen on cell cycle progression of synchronous MCF-7 human mammary carcinoma cells, Cancer Research. *43:* 4007-4010, 1983.

25. Furman, E., Rushkin, E, Margalit, R, Bendel, P and Degani, H Tamoxifen induced changes in MCF7 human breast cancer: *in vitro* and *in vivo* studies using nuclear magnetic resonance spectroscopy and imaging, Steroid biochem mole biol. *43:* 189-195, 1992.

26. Neeman, M., and Degani, H Metabolic studies of estrogen- and tamoxifen-treated human breast cancer cells by nuclear magnetic resonance spectroscopy, Cancer Research. *49:* 589-594, 1989.

27. Neeman, M., and Degani, H Early estrogen induced metabolic changes and their inhibition by actinomycin-D and cycloheximide in human breast cancer cells: ^{31}P and ^{13}C NMR studies., Proc Natl Acad Sci. *86:* 5585-5589, 1989.

28. Ruiz-Cabello, J., Berghmans, K, Kaplan, O, Lippman, M E, Clarke, R, and Cohen, J A Hormone dependence of breast cancer cells and the effects of tamoxifen and estrogen: ^{31}P NMR studies, Breast Cancer Research and Treatment. *33:* 209-217, 1995.

29. Thomas, M., Monet, J, Brami, M, Dautigny, N, Assailly, J, Ulmann, A, and Bader, C A Comparative effects of 17β-estradiol, progestin R5020, tamoxifen and RU38486 on lactate dehydrogenase activity in MCF-7 human breast cancer cells, J Steroid Biochem. *32:* 271-277, 1989.

30. Dehdashti, F., Flanagan, F L, Mortimer, J E, Katzenellenbogen, J A, Welch, M J, and Siegel, B A Positron emission tomorgraphic assessment of "metabolic flare" to predict response of metastatic breast cancer to antiestrogen therapy, Eur J Nucl Med. *26:* 51-56, 1999.

31. Evans, S. M., Koch, C J, Laughlin, K M, Jenkins, W T, Van Winkle, T, and Wilson, D F Tamoxifen induces hypoxia in MCF-7 xenografts, Cancer Research. *57:* 5155-5161, 1997.

32. Furman-Haran, E., Margalit, R, Grobeld, D, and Degani, H Dynamic contrast-enhanced magnetic resonance imaging reveals stress-induced angiogenesis in MCF7 human breast tumors, Proc Natl Acad Sci. *93:* 6247-6251, 1996.

33. Gagliardi, A. R., and Collins, D C Inhibition of angiogenesis by antiestrogens, Cancer Research. *53:* 533-535, 1993.

34. Gagliardi, A. R., Hennig, B, and Collins, D C Antiestrogens inhibit endothelial cell growth stimulated by angiogenic growth factors, Anticancer Research. *16:* 1101-1106, 1996.

35. Gasparini, G., Fox, S B, Verderio, P, Bonoldi, E, Bevilacqua, P, Boracchi, P, Dante, S, Marubini, E, and Harris, A L Determination of angiogenesis adds information to estrogen receptor status in predicting the efficacy of adjuvant tamoxifen in node-positive breast cancer patients, Clinical Cancer Research. *2:* 1191-1198, 1996.

36. Lindner, D. J., and Borden, E C Effects of tamoxifen and interferon-β or the combination on tumor-induced angiogenesis, Int J Cancer. *71:* 456-461, 1997.

37. Lin, A. A., Nguyen, T, and Miller, W M A rapid method for counting cell nuclei using a particle sizer/counter, Biotechnology Techniques. *5:* 153-156, 1991.

38. Katzenellenbogen, B. S., Norman, M J, Eckert, R L, Peltz, S W and Mangel, W F Bioactivities, estrogen receptor interactions, and plasminogen activator-inducing activities of tamoxifen and hydroxytamoxifen isomers in MCF-7 human breast cancer cells, Cancer Research. *44:* 112-119, 1984.

39.   Lippman, M., Bolan, G, and Huff, K The effects of estrogens and antiestrogens on hormone-responsive human breast cancer in long-term tissue culture., Cancer Research. *36:* 4595-4601, 1976.

40.   Taylor, C. M., Blanchard, B, and Zava, D T Estrogen Receptor-mediated and cytotoxic effects of the antiestrogens tamoxifen and 4-hydroxytamoxifen, Cancer Research. *44:* 1409-1414, 1984.

41.   Villalobos, M., Aranda, M, Nunez, M I, Becerra, D, Olea, N Tuiz de Almodovar, M , and Pedraza, V Interaction between ionizing radiation, estrogens and antiestrogens in the modification of tumor microenvironment in estrogen dependent multicellular spheroids, Acta Oncologia. *34:* 413-417, 1995.

42.   Mueller-Holzner, E., Marth, C, Zeimet, AG, Hofstader, F, Daxenbichler, G Effects of sex- and glucocorticoid steroids on breast cancer cells grown as either multicellular tumor spheroids or monolayers, J Steroid Biochem Mol Biol. *58:* 13-19, 1996.

43.   Arafah, B., Griffin, P, Gordon, N, and Pearson, O Influence of tamoxifen and estradiol on the growth of human breast cancer cells in vitro., Cancer Research. *46:* 3268-3272, 1986.

44.   Leonessa, F., Jacobson, M, Boyle, B, Lippman, J, McGarvey, M, and Clarke, R Effect of tamoxifen on the multidrug-resistant phenotype in human breast cancer cells: isobologram, drug accumulation, and Mr 170,000 glycoprotein (gp170) binding sites, Cancer Research. *54:* 441-447, 1994.

45.   Bourrat-Floeck, B., Groebe, K, and Mueller-Klieser, W Biological response of multicellular EMT6 spheroids to exogenous lactate, Int J Cancer. *47:* 792-799, 1991.

46. Sauer, L. A., and Dauchy, R T Regulation of lactate production and utilization in rat tumors *in vivo*, J Biol Chem. *260:* 7496-7501, 1985.

47. Sauer, L. A., and Dauchy, R T *In vivo* lactate production and utilization by Jensen sarcoma and Morris hepatoma, Cancer Research. *46:* 689-693, 1986.

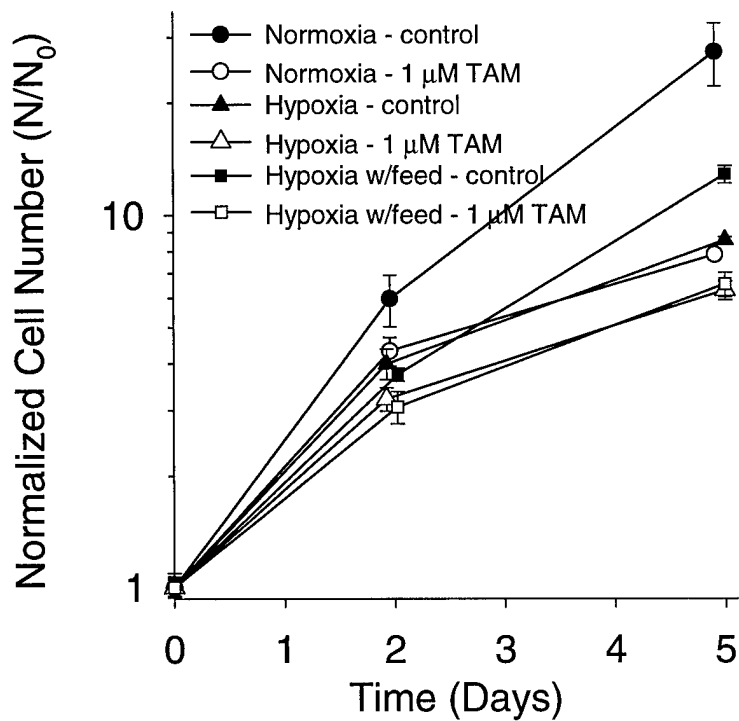48. Warburg, O., Science. *124:* 269-270, 1956.

Figure 1. Cell proliferation as a function of time for MCF7 human breast cancer cells cultured on microcarriers under normoxic conditions (20% oxygen), hypoxic conditions (2% oxygen), and hypoxic conditions with media replenishment on day 3. Each point represents the mean of six different measurements from two independent experiments. Filled shapes represent flasks treated with vehicle control (0.1% ethanol). Open shapes represent flasks treated with 1μM TAM.
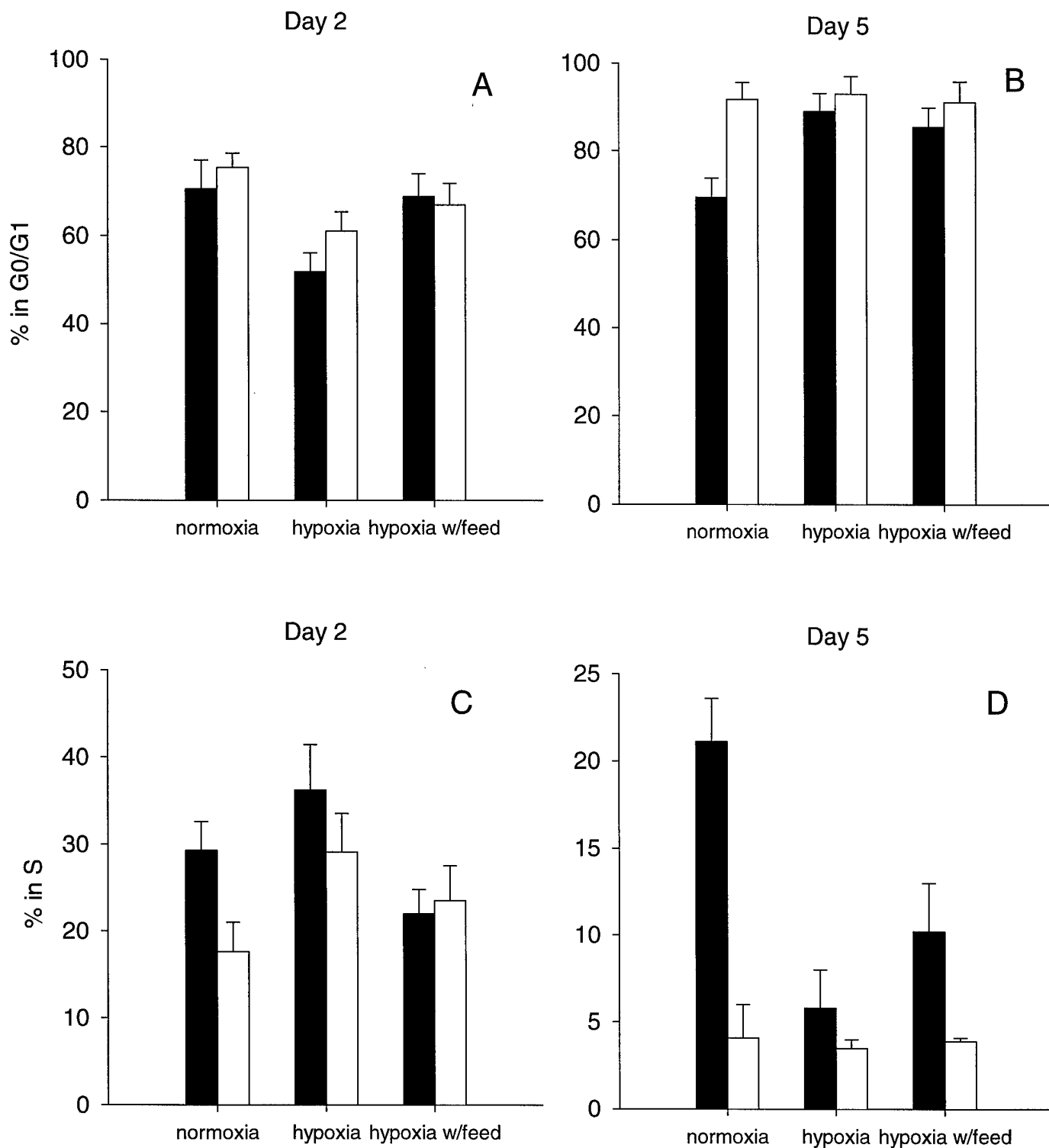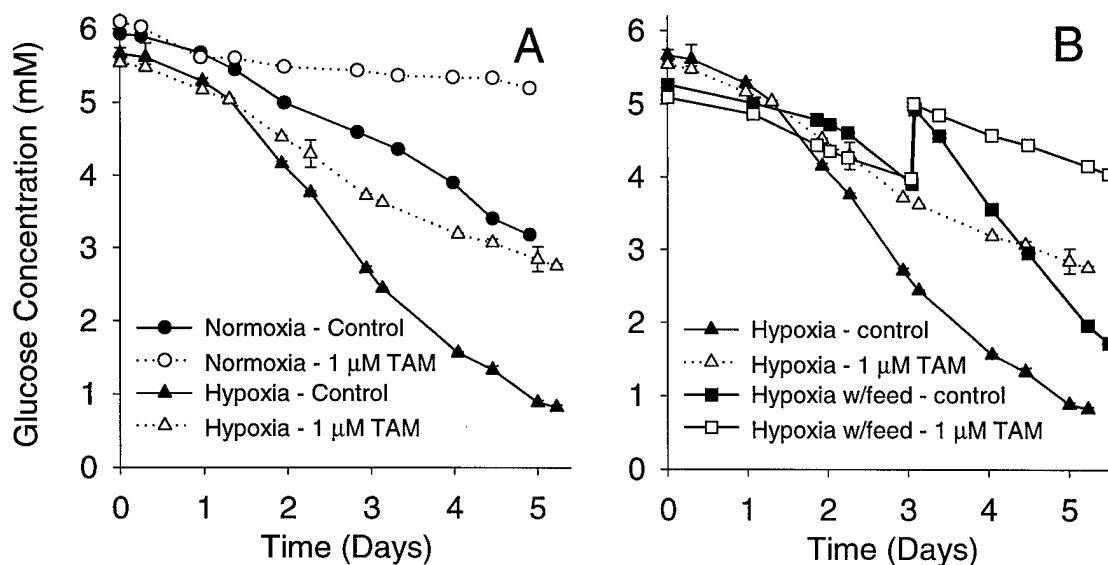
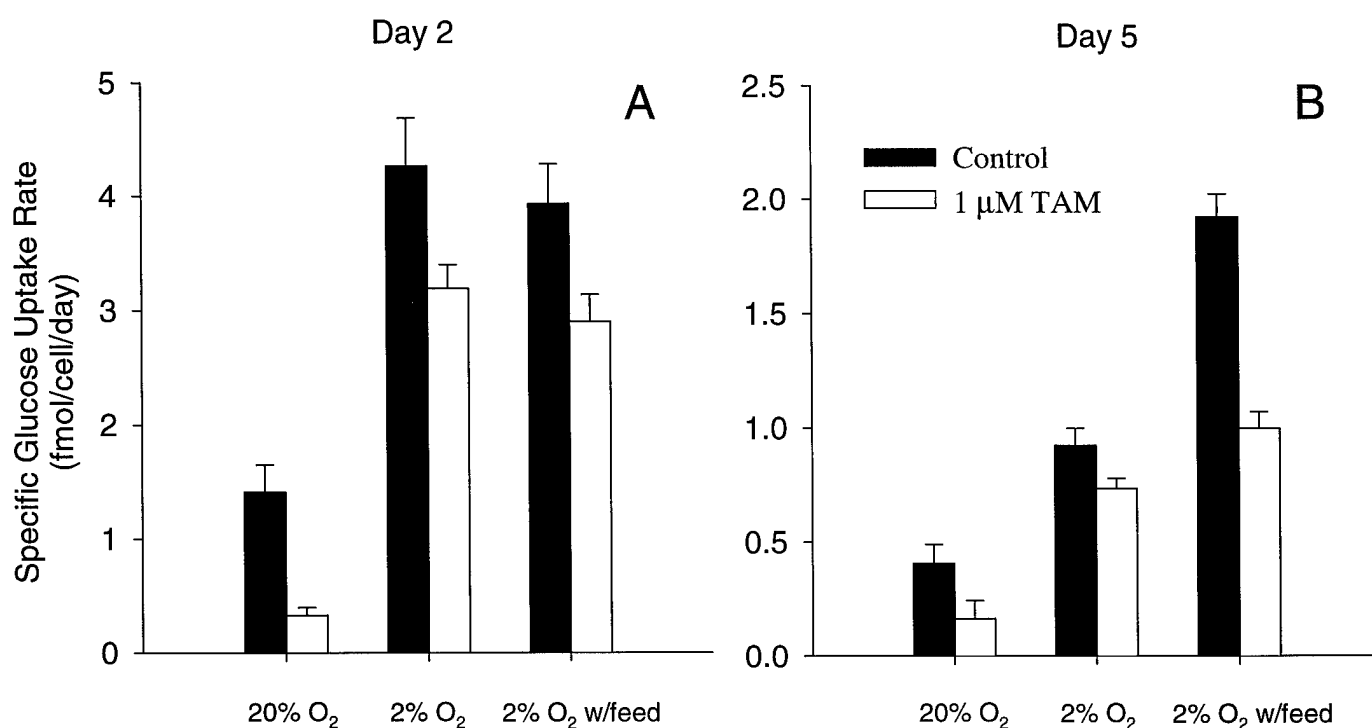Figure 2. Cell cycle distribution on days 2 (A,C) and 5 (B,D) for MCF7 human breast cancer cells under normoxic conditions (20% oxygen), hypoxic conditions (2% oxygen), and hypoxic conditions with media replenishment on day 3. Percent in phase G0/G1 (A,B) and S (C,D) is presented as the mean ± S.D. of six measurements from two independent experiments. Black bars represent flasks treated with vehicle control (0.1% ethanol). White bars represent flasks treated with 1μM TAM.
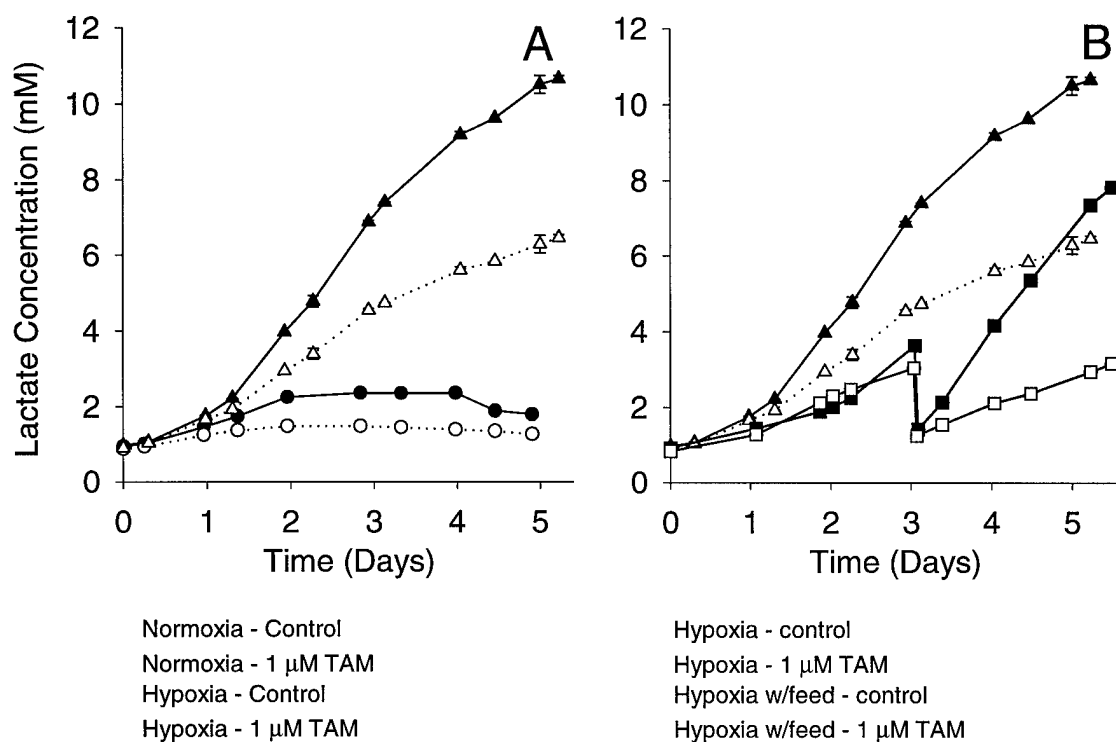
Figure 3. Glucose concentrations as a function of time. Normoxic conditions (20% oxygen) and hypoxic conditions (2% oxygen) are compared in panel A. Effect of media replenishment on day 3 under hypoxic conditions is examined in panel B. Metabolite concentrations are presented as the mean ± S.D. of six measurements from a representative experiment. Filled shapes represent flasks treated with vehicle control (0.1% ethanol). Open shapes represent flasks treated with 1μM TAM.
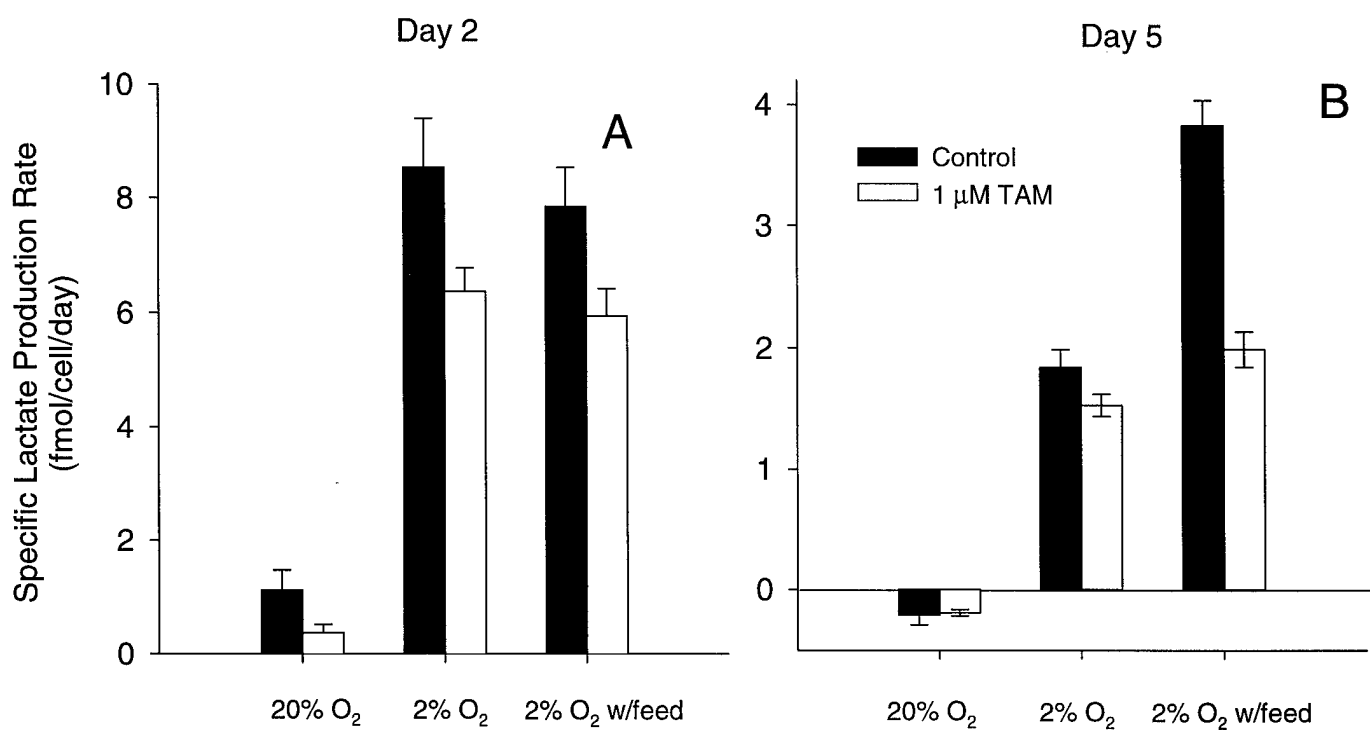
Figure 4. Specific glucose uptake rates on days 2 (A) and 5 (B) for MCF7 cells under normoxic conditions (20% oxygen), hypoxic conditions (2% oxygen), and hypoxic conditions with media replenishment on day 3. Uptake rates are presented as the mean ± S.D. of six measurements from two independent experiments. Black bars represent flasks treated with vehicle control (0.1% ethanol). White bars represent flasks treated with 1μM TAM.
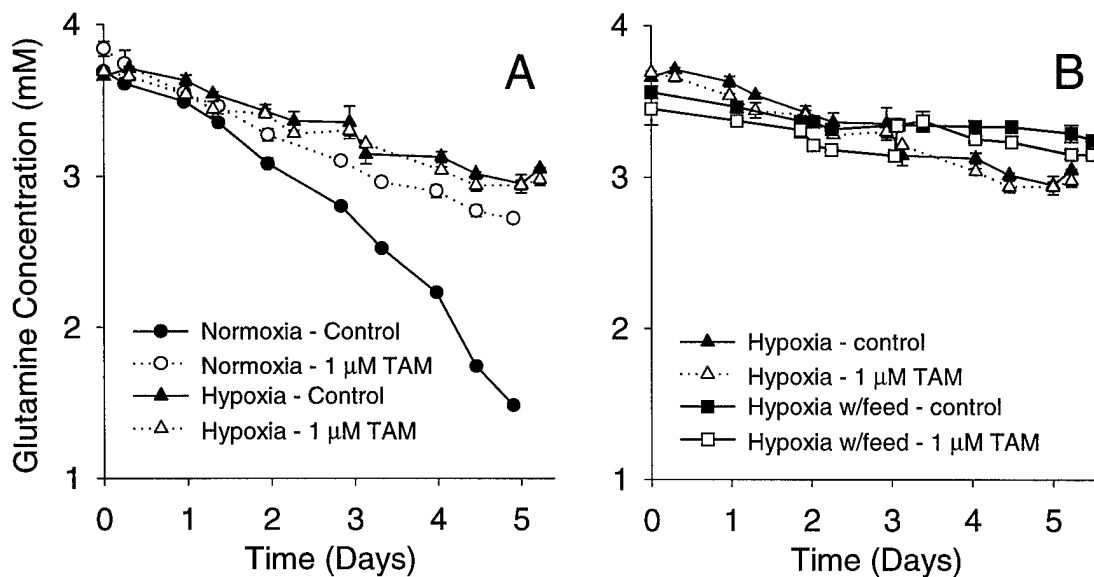
Figure 5. Lactate concentrations as a function of time. Normoxic conditions (20% oxygen) and hypoxic conditions (2% oxygen) are compared in panel A. Effect of media replenishment on day 3 under hypoxic conditions is examined in panel B. Metabolite concentrations are presented as the mean ± S.D. of six measurements from a representative experiment. Filled shapes represent flasks treated with vehicle control (0.1% ethanol). Open shapes represent flasks treated with 1μM TAM.

Figure 6. Specific lactate production rates on days 2 (A) and 5 (B) for MCF7 cells under normoxic conditions (20% oxygen), hypoxic conditions (2% oxygen), and hypoxic conditions with media replenishment on day 3. Negative values represent lactate utilization. Uptake rates are presented as the mean ± S.D. of six measurements from two independent experiments. Black bars represent flasks treated with vehicle control (0.1% ethanol). White bars represent flasks treated with 1μM TAM.

Figure 7. Glutamine concentrations as a function of time. Normoxic conditions (20% oxygen) and hypoxic conditions (2% oxygen) are compared in panel A. Effect of media replenishment on day 3 under hypoxic conditions is examined in panel B. Metabolite concentrations are presented as the mean ± S.D. of six measurements from a representative experiment. Filled shapes represent flasks treated with vehicle control (0.1% ethanol). Open shapes represent flasks treated with 1μM TAM.
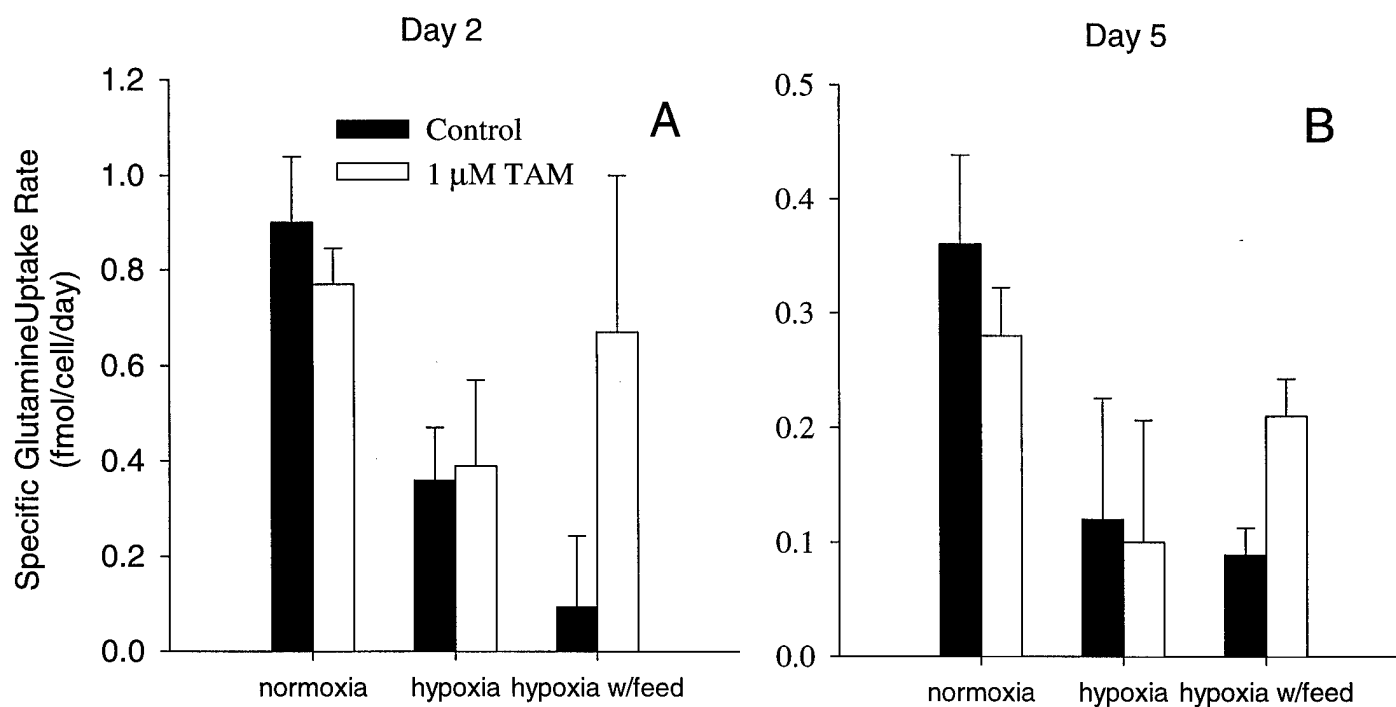
Figure 8. Specific glutamine uptake rates on days 2 (A) and 5 (B) for MCF7 cells under normoxic conditions (20% oxygen), hypoxic conditions (2% oxygen), and hypoxic conditions with media replenishment on day 3. Uptake rates are presented as the mean ± S.D. of six measurements from two independent experiments. Black bars represent flasks treated with vehicle control (0.1% ethanol). White bars represent flasks treated with 1μM TAM.
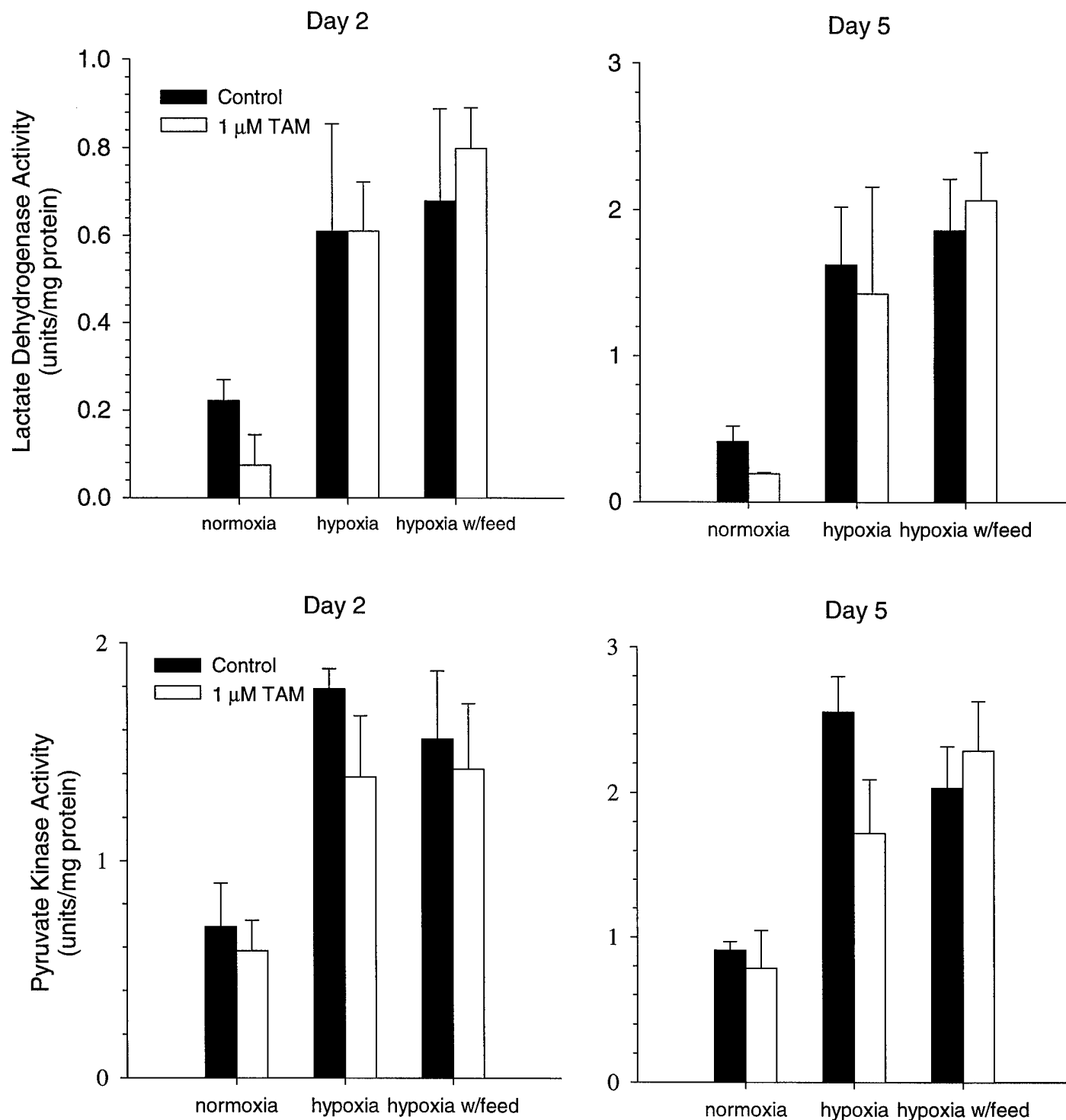
Figure 9. Enzyme activity on days 2 (A,C) and 5 (B,D) for MCF7 cells under normoxic conditions (20% oxygen), hypoxic conditions (2% oxygen), and hypoxic conditions with media replenishment on day 3. LDH activity is shown in panels A and B. PK activity is shown in panels C and D. Uptake rates are presented as the mean ± S.D. of six measurements from two independent experiments. Black bars represent flasks treated with vehicle control (0.1% ethanol). White bars represent flasks treated with 1µM TAM.